The Asian Summer Monsoon: An Intercomparison of CMIP5 vs. CMIP3 Simulations of the Late 20th Century

K. R. Sperber[1*], H. Annamalai[2], I.-S. Kang[3], A. Kitoh[4], A. Moise[5], A. Turner[6], B. Wang[2], and T. Zhou[7]

Climate Dynamics
(Accepted: November 18, 2012)

[1*]Program for Climate Model Diagnosis and Intercomparison
Lawrence Livermore National Laboratory
P.O. Box 808, L-103
Livermore, CA 94551
Ph: 925-422-7720
Email: sperber1@llnl.gov

[2]International Pacific Research Center
School of Ocean and Earth Science and Technology
1680 East-West Road
University of Hawaii
Honolulu, Hawaii 96822

[3]School of Earth and Environmental Science (SEES)
Seoul National University
Seoul 151-742, Korea

[4]Meteorological Research Institute
1-1 Nagamine, Tsukuba-shi, Ibaraki Pref.
305-0052 Japan

[5]Climate Variability and Change Group
Centre for Australian Weather and Climate Research
Australian Bureau of Meteorology
PO Box 1289, Melbourne, VIC 3001, Australia

[6]National Centre for Atmospheric Science-Climate
Department of Meteorology
University of Reading
Reading RG6 6BB
United Kingdom

[7]LASG, Institute of Atmospheric Physics
Chinese Academy of Sciences
P.O. Box 9804
Beijing 100029, China

[*]Corresponding Author

Abstract The boreal summer Asian monsoon has been evaluated in 25 Coupled Model Intercomparison Project-5 (CMIP5) and 22 CMIP3 GCM simulations of the late 20th Century. Diagnostics and skill metrics have been calculated to assess the time-mean, climatological annual cycle, interannual variability, and intraseasonal variability. Progress has been made in modeling these aspects of the monsoon, though there is no single model that best represents all of these aspects of the monsoon. The CMIP5 multi-model mean (MMM) is more skillful than the CMIP3 MMM for all diagnostics in terms of the skill of simulating pattern correlations with respect to observations. Additionally, for rainfall/convection the MMM outperforms the individual models for the time mean, the interannual variability of the East Asian monsoon, and intraseasonal variability. The pattern correlation of the time (pentad) of monsoon peak and withdrawal is better simulated than that of monsoon onset. The onset of the monsoon over India is typically too late in the models. The extension of the monsoon over eastern China, Korea, and Japan is underestimated, while it is overestimated over the subtropical western/central Pacific Ocean. The anti-correlation between anomalies of all-India rainfall and Niño3.4 sea surface temperature is overly strong in CMIP3 and typically too weak in CMIP5. For both the ENSO-monsoon teleconnection and the East Asian zonal wind-rainfall teleconnection, the MMM interannual rainfall anomalies are weak compared to observations. Though simulation of intraseasonal variability remains problematic, several models show improved skill at representing the northward propagation of convection and the development of the tilted band of convection that extends from India to the equatorial west Pacific. The MMM also well represents the space-time evolution of intraseasonal outgoing longwave radiation anomalies. Caution is necessary when using GPCP and CMAP rainfall to validate (1) the time-mean rainfall, as there are systematic differences over ocean and land between these two data sets, and (2) the timing of monsoon withdrawal over India, where the smooth southward progression seen in India Meteorological Department data is better realized in CMAP data compared to GPCP data.

Keywords Asian summer monsoon; Climate model; Intercomparison; Model Systematic Error; Skill Metrics

1 Introduction

Nearly half of the world's population is dependent on monsoon rainfall for food and energy security. The monsoon is an integral and robust component of the seasonal cycle, though the vagaries of its timing, duration, and intensity are of major concern, especially over semi-arid regions where agriculture is the primary source of food. On interannual time scales the standard deviation of the Indian/South Asian monsoon rainfall is on the order of 10% of the seasonal mean, and the corresponding percentage of East Asian summer monsoon rainfall is ~30% (Zhou and Yu 2005). However, subseasonal variations can give rise to much greater swings in rainfall variability and modulate higher frequency variations, including tropical cyclones (e.g. Nakazawa 1986). Recent examples of such extreme swings in the monsoon include the July 2002 drought over India (Prasanna and Annamalai 2012), and the Pakistan flood of July-August 2010 (Lau and Kim 2010). Forewarning of extreme subseasonal variations is particularly important, since this would enable the selection of alternative crops, the adjustment of planting times, and management of hydrometeorological services (water distribution, etc.) to help cope with the extreme conditions (Webster and Jian 2011). Improvement in the prospects of monsoon predictability at all time scales requires (1) an improved understanding of the physical processes that modulate the monsoon, (2) improved observations for processes studies, initialization of forecast models, and long term monitoring, and (3) better simulation of the monsoon in numerical weather prediction models and climate models.

There are many facets of the atmosphere-ocean-land-cryosphere system that interact to produce monsoon. The seasonal cycle of solar forcing is the basic driver of the monsoon over the Asian region, contributing to the development of a land-sea temperature gradient, including aloft, due to heating of the Tibetan Plateau (Li and Yanai 1996; Webster et al. 1998). The temperature and sea-level pressure gradients that develop promote the formation of the low-level cross-equatorial southwest monsoon circulation (Findlater 1970). This circulation transports moisture laden air from the ocean to feed convection (Pearce and Mohanty 1984) that leads to the onset of the monsoon. Subsequently, the off-equatorial convective heating interacts with the circulation to help maintain monsoon rainfall (Gill 1980; Annamalai and Sperber 2005).

Precursory and/or contemporaneous forcings, such as those related to snowcover (Blanford 1884), and pressure over the Pacific and Indian Oceans (Walker 1924), suggested evidence that teleconnections from remote regions could influence the monsoon, and be a source of predictability. Potential prediction of such slowly varying components of the climate system, especially sea surface temperature (SST; Charney and Shukla 1981), form the basis of seasonal prediction systems with dynamical models and empirical/statistical models. The main skill in seasonal forecasting of the monsoon is intimately linked to our ability to forecast the El Niño/Southern Oscillation (ENSO). However, properly representing the location and intensity of the ENSO diabatic heating is essential for getting a response consistent with that expected from statistical teleconnections relationships (Slingo and Annamalai 2000). Other more local interactions, such as Indian Ocean variations (Boschat et al. 2012) and soil moisture (Webster et al. 1998), may play a role in modulating the monsoon.

Given the multitude of physical processes and interactions that influence the monsoon, it is no wonder that simulation and prediction of the monsoon remain grand challenge problems. The challenges of modeling the monsoon and making climate change projections have been discussed in Turner et al. (2011) and Turner and Annamalai (2012). By its very nature, simulating the monsoon requires models with coupling between the atmosphere, the ocean, and land. In prescribed SST experiments, such as from the Tropical Ocean Global Atmosphere Monsoon Experimentation Group (WCRP 1992, 1993), the Atmospheric Model Intercomparison Project (Sperber and Palmer 1996), and the Climate Variability and Predictability (CLIVAR) Climate of the 20^{th} Century simulations (Zhou et al. 2009a) observed interannual variations of Asian-Australian monsoon rainfall over land were poorly represented. This in part occurred because of the use of prescribed SST's, which forced an incorrect rainfall-SST teleconnection (Wang et al. 2004). Ocean-atmosphere coupling also gives rise to a wide-range of model performance, in which monsoon climate and variability can be adversely affected by poorly representing air-sea interaction and its relationship to evaporation (Bollasina and Nigam 2009). Even so, incremental progress in simulating monsoon has been hard-fought due to improvements in local, regional, and global interactions that modulate the monsoon on diurnal through interdecadal time scales (e.g. Wang 2006).

The goal of this paper is to assess the fidelity of boreal summer Asian monsoon in the Coupled Model Intercomparison Project-5 (CMIP5) models as compared to the CMIP3 models and observations. We employ a multitude of diagnostics and skill metrics to present a quantitative assessment of the models' monsoon performance relative to observations. The diagnostics were selected after much deliberation by the CLIVAR Asian-Australian Monsoon Panel (AAMP) Diagnostics Task Team, and helpful comments from the AAMP membership and other experts. The accompanying skill scores are meant to provide a broad overview of the ability to simulate the Asian summer monsoon, though analysis at the process-level is beyond the scope of this assessment. We will, however, discuss possible physical interpretations of the main results. The models and observations are discussed in Section 2. We evaluate the time-mean rainfall and 850hPa wind in Section 3, and the climatological annual cycle and timing of monsoon onset, peak, withdrawal, and duration are explored in Section 4. The interannual variability of the ENSO-monsoon teleconnection, and teleconnections to the 850hPa zonal wind over East Asia are given in Section 5. Boreal summer intraseasonal variability (BSISV) is evaluated in Section 6, and discussion and conclusions are given in Section 7.

2 Models, Observations, and Skill Scores

Table 1 contains basic information on the CMIP5 (Taylor et al. 2012) and CMIP3 models (Meehl et al. 2007) used in this study, including horizontal and vertical resolution of the atmospheric and oceanic components. The CMIP5 models were developed circa 2011, while the CMIP3 models were developed circa 2004. To more easily discriminate between the two vintages of models in this paper, the model designations for the CMIP5 models are capitalized, while the model designations of the CMIP3 models are given as lower-case. Single realizations for each of the models have been evaluated using the historical simulations from CMIP5 and the Climate of the 20^{th} Century (20c3m) simulations from CMIP3. Though the simulation period is ~1850-present, the period 1961-99 is analyzed herein. This is the period when both CMIP5 and CMIP3 had high-

frequency (daily) data with which to evaluate intraseasonal variability and the climatological annual cycle of pentad rainfall. Thus, the analysis period of the high-frequency variability is consistent with the analysis period of the interannual variability and the climatological performance derived from monthly data. These simulations include the modeling groups best estimates of natural (e.g. solar irradiance, volcanic aerosols) and anthropogenic (e.g. greenhouse gases, sulfate aerosols, ozone) climate forcing during the simulation period. Compared to CMIP3, the CMIP5 models typically have higher horizontal and vertical resolution in the atmosphere and ocean, a more detailed treatment of aerosols, and some have a more complete representation of the Earth system (e.g. carbon cycle). Detailed documentation of the CMIP3 models can be found at:
http://www-pcmdi.llnl.gov/ipcc/model_documentation/ipcc_model_documentation.php
and CMIP5 model documentation can be found at:
http://www.earthsystemgrid.org/search?Type=Simulation+Metadata

In most cases, multiple sources of observations are used in our analysis. For rainfall we use the Global Precipitation Climatology Project (GPCP) data (Huffman et al., 2001) and the Climate Prediction Center Merged Analysis of Precipitation (CMAP; Xie and Arkin 1997) for 1979-2007. Advanced Very-High Resolution Radiometer daily outgoing longwave radiation for 1979-2006 (AVHRR OLR, Liebmann and Smith 1996), which is a good proxy of tropical convection (Arkin and Ardanuy 1989), is used to validate intraseasonal variability. For the 850hPa wind we use the Japan Meteorological Agency and the Central Research Institute of Electric Power Industry Reanalysis-25 (JRA-25; Onogi et al. 2007) for 1979-2007, the European Centre for Medium-Range Weather Forecasts Reanalysis-40 (ERA40; Uppala et al. 2005) for 1961-1999, and the National Centers for Environmental Prediction/National Center for Atmospheric Research Reanalysis (NCEP/NCAR; Kalnay et al. 1996) for 1961-2007.

Model skill is calculated against a primary observational data set, for example, GPCP in the case of precipitation. Given that the observations are only estimates of the true values, we also calculate the skill between the different sets of observations. This observational skill estimate is a measure of consistency between the two sets of observations. The model skill is predominantly assessed using pattern correlation between the models and observations. Space-time correlation is used to assess the life cycle of the model and observed intraseasonal variability. Correlation of anomalies of all-India rainfall (AIR) and Niño3.4 SST is one skill metric used to assess the ENSO-monsoon relationship, and the threat score and hit-rate are used to assess how well the models represent the observed spatial extent of the monsoon domain. The skill scores for the individual models and the multi-model means (MMM's) are presented in scatter plots, and the numerical values are given in Tables 2 and 3. For the calculation of the skill metrics, the model data have been regridded to a 2.5^{o} x 2.5^{o} grid (144 x 73 for winds and OLR (the AVHRR grid), and 144 x 72 for precipitation (the grid of GPCP and CMAP). More details of the skill scores are presented in the relevant sections of the paper.

Due to the large number of models evaluated, in this paper we only present spatial patterns of the diagnostics for the observations, for the two models that demonstrate the range of performance based on the relevant skill score, and for the CMIP5 and CMIP3

MMM's. To facilitate evaluation by the modeling groups and other interested parties, we have posted figures for all of the models for each of the diagnostics at: http://www-pcmdi.llnl.gov/projects/ken/cmip5_bsisv/Tables.html

3 Time-mean State

The June-September time-mean patterns of rainfall and 850hPa wind represent key aspects of the monsoon. The intense solar heating in late spring and early summer supports the development of a heat low over the land of south and Southeast Asia. The resulting land-sea thermal and pressure gradients induce the development of cross-equatorial low-level winds that transport an increased flux of moisture onto the Asian landmass, heralding the onset of the monsoon. The strong coupling between diabatic heating and the circulation further amplifies the cross-equatorial flow, the moisture influx, and the rainfall. The orographic structure of the Asian landmass provides anchor points where the observed monsoon rainfall tends to be concentrated, especially adjacent to the Western Ghats, the foothills of the Himalayas, the Burmese coast, and the Philippines (Fig. 1a). The orography also plays an important role in anchoring the intensity and position of the cross-equatorial flow (Hoskins and Rodwell 1995). Thus, apart from realistic representation of physical processes, the details of the vertical representation of orography and its interaction with the circulation are important for realistic simulation of regional rainfall in models. With a pattern correlation of 0.93 between GPCP and CMAP rainfall, the spatial distribution of observed rainfall is well established (Table 2). The vagaries in simulating the multitude of physical processes involved in the monsoon leads to diversity in the ability to simulate the observed rainfall distribution, as seen in Figs. 1b and 1c. Despite gridscale noise at its native horizontal resolution (Fig. 1b), when regridded to the observational horizontal resolution (not shown), the CNRM-CM5 model has the highest pattern correlation with GPCP rainfall. This model over-emphasizes the monsoon rainfall over the tropical oceans and does not capture the local maxima over central India. The MIROC-ESM model, Fig. 1c, has the smallest pattern correlation with GPCP rainfall, and it overestimates the rainfall over the Arabian Sea, and it underestimates the East Asian component of the monsoon.

The MMM is an efficient way to assess the overall performance of the CMIP5 and CMIP3 models. For both sets of integrations, the MMM outperforms the individual models in terms of the pattern correlation skill metric (Table 1). Figures 1d and 1e indicate that the CMIP5 MMM has an improved representation of rainfall compared to the CMIP3 MMM. This is reflected by the more realistic magnitude of rainfall adjacent to the Western Ghats, the foothills of the Himalayas, and adjacent to the Philippines. The enhanced skill in representing the precipitation anchor points in the CMIP5 models may be associated with their higher horizontal resolution compared to the CMIP3 models. Even so, the MMM's have smaller pattern correlations than that between GPCP and CMAP, indicating scope for model improvement in the representation of rainfall.

Figures 1f-1j show the spatial distributions of the rainfall errors. The magnitude of the rainfall errors in individual models (Figs. 1g and 1h) is larger than seen in observations (Fig. 1f) and the MMM's (Figs. 1i-1j). The CMIP5 and CMIP3 MMM errors have virtually the same spatial structure, with an underestimate of rainfall over the Asian continent from India to Southeast Asia, and extending north over eastern China, Korea, and southern Japan. The error over eastern China, Korea, and Japan indicates that rainfall in the Meiyu front is underestimated. Alternatively, the rainfall is over-estimated over most of the tropical western/central Indian Ocean. Over the western Pacific, there is a tripole error pattern from the equator to 45^{o}N. The MMM error structure is largely consistent with difference between CMAP and GPCP (Fig. 1f). A similar error structure is also seen by comparing Tropical Rainfall Measurement Mission rainfall with GPCP (Brian Mapes, personal communication, 2012), suggesting that the lack of definitive precipitation intensity estimates may be an impediment to making further progress in simulating monsoon rainfall.

The observed and simulated time-mean 850hPa wind is given in Fig. 2. Skill is calculated with respect to ERA40. The ERA40 and JRA25 reanalysis (not shown) estimates of the wind structure are highly consistent, as indicated by their pattern correlation of 0.99 (Table 2). The main features of the low-level monsoon circulation include the cross-equatorial flow over the western Indian Ocean/East African highlands, the westerly flow that extends from the Arabian Sea to the South China Sea, the monsoon trough over the Bay of Bengal, and the weak southerlies over the South China Sea and East Asia. The difference between JRA25 and ERA40, seen in Fig. 2f (note the different unit vector scale relative to the full field in Fig. 2a), is smaller than that between the NCEP-NCAR and ERA15 reanalyses (Annamalai et al. 1999), where there were also large errors over the tropical Indian Ocean. The simulated northwesterly wind error over the Arabian Peninsula, and the northerly error over Pakistan and the Thar Desert, Figs. 2g-2j, is similar to the differences between the reanalyses (Fig. 2f). This suggests that improved observations are needed to constrain the climate simulations. It is possible that a dearth of rawindsonde reports from remote regions, in conjunction with the way in which the land surface processes and/or orography are handled, may contribute to the observational uncertainty over the land from the reanalyses.

As for rainfall, the MMM's (Figs. 2d and 2e) outperform the range of model behavior (Figs. 2b and 2c), and the systematic model error is nearly identical between CMIP5 and CMIP3 (Figs. 2i and 2j). The MMM wind error is consistent with the rainfall error, with weak flow over India and the Bay of Bengal being associated with the underestimated rainfall over these locations. Despite overly strong rainfall over the western Arabian Sea, both CMIP5 and CMIP3 MMM's suggest that the underestimated cross-equatorial flow is associated with the underestimated off-equatorial diabatic heating anomalies along the monsoon trough, near 20^{o}N. The monsoon trough over the Bay of Bengal is too zonal (Figs. 2d and 2e), which may contribute to the excessive rainfall in the vicinity of the South China Sea and Maritime Continent (Figs. 1d and 1e). Support for this scenario has been found in experiments using the GFDL AM2.1 model (Annamalai et al. 2012a). However, the sequence of events that give rise to these errors needs to be worked out: Is it the poor development of the monsoon trough that gives rise to the excessive rainfall near the Maritime Continent, or does excessive rainfall near the Maritime Continent result in a poor representation of the monsoon trough? Alternative and/or additional interactions/feedbacks need to be considered in the development of the systematic error, including the possible role of Rossby wave descent over South Asia (Annamalai and Sperber 2005), SST feedback, and moisture transports.

Over the western Pacific the simulated cyclonic wind error (Figs. 2g-2j), which is consistent with the rainfall overestimate seen near 120^{o}E-180^{o}E, 8^{o}N-22^{o}N (Figs. 1g and 1i-1j; PCM rainfall error not shown), indicates a large bias in the simulation of the western Pacific subtropical high. The northeasterly wind error along the poleward flank of this cyclonic circulation pattern and the northerly error over the South China Sea are indicative of lower moisture content air (Prasanna and Annamalai 2012) and reduced rainfall along the Meiyu, Changma, Baiu rainfall front. For the MMM's, the time mean wind and the wind error oppose each other, suggesting that reduced moisture from monsoon westerlies and the southerlies over the South China Sea is a contributing factor in the weak Meiyu, Changma, Baiu front. However, in the case of PCM, the time-mean wind and the wind error (Figs. 2b and 2h) are both easterly/northeasterly near southern Japan and China, suggesting that advection of lower moisture air from the extratropics is a factor in producing the weak Meiyu, Changma, Baiu front.

The overall skill in simulating the time-mean monsoon is given in Fig. 3, which is a scatterplot of the pattern correlation relative to observations (ERA-40 and GPCP) for 850hPa wind vs. precipitation. The results indicate that for all models the 850hPa wind is better simulated than the precipitation. This is perhaps not surprising since the circulation is a response to integrated diabatic heating and not to the details of the regional rainfall distribution. For 850hPa wind, the MMM and CNRM-CM5 skill are within the range of observational skill when NCEP/NCAR Reanalysis wind is also considered. Importantly, for both CMIP5 and CMIP3 there is a better than 1% statistically significant relationship between the skill in representing the rainfall and the 850hPa wind. For example, the CNRM-CM5 had the largest pattern correlation with observations for both rainfall and 850hPa wind (Table 2). The statistical relationship suggests that improving the rainfall in the models will result in an improved representation of the wind and vice versa.

4 Annual Cycle

In this section we evaluate the annual cycle of rainfall using climatologies of both monthly data and pentad data. The monthly data are used to generate latitude-time plots to assess how well the models represent the annual cycle of rainfall in the vicinity of India, including the northward propagation of the continental rainband. The pentad data are used to assess how well the models represent the time of monsoon onset, peak, withdrawal, and the duration of the monsoon season, as well as the spatial extent of the monsoon domain.

4.1 Indian Monsoon

A latitude-time diagram of monthly rainfall, averaged between 70^{o}E-90^{o}E, is constructed to show the transition of rainfall between the ocean and the Indian subcontinent during the course of the annual cycle. The GPCP and CMAP observations (Figs. 4a and 4b, respectively) show the development of two rainfall maxima beginning in May. The poleward branch depicts the evolution of the Indian monsoon, with the maximum rainfall occurring in July. The oceanic branch, located near 5^{o}S, reaches a local maximum in September, as the Indian monsoon weakens. These features are consistent between GPCP and CMAP, with a pattern correlation of 0.89 over the domain 10^{o}S-30^{o}N for May-October (see box in Fig 4a). However, CMAP is drier (wetter) than GPCP over India (the tropical Indian Ocean), consistent with the observational biases noted for the time mean state (see Fig. 1, Section 3). Furthermore, these biases in the distribution of land vs. oceanic rainfall also give rise to uncertainty in the latitude of maximum rainfall over India during the boreal summer in GPCP and CMAP.

The latitude-time plots for MIROC5 and csiro-mk3.5 show the range of model skill in representing the annual cycle of rainfall over the Indian longitudes (Figs. 4c and 4d), based on pattern correlation skill over the afore-mentioned space-time domain. MIROC5 overestimates the magnitude of the Indian monsoon and oceanic rainfall bands. The oceanic rainband and the rainfall minimum to its north are not as coherent as observed, contributing to a pattern correlation of 0.78 relative to GPCP. csiro-mk3.5 has a late development of the Indian monsoon, and the oceanic rainband transitions into the Northern Hemisphere during boreal summer, unlike the observations. With such biases, csiro-mk3.5 only has a pattern correlation of 0.17 with GPCP.

The CMIP5 and CMIP3 MMM's (Figs. 4e and 4f) have nearly identical pattern correlations with GPCP (0.67 and 0.66, respectively). The MMM's indicate that the core of the continental rainband does not propagate as far north as observed, consistent with the model biases seen of other modeling studies (Gadgil and Sajani 1998; Rajeevan and Najundiah 2009). Additionally, both MMM fail to capture the observed northward propagation of the rainfall minimum from the equator to 10^{o}N during boreal summer, and the oceanic rainband is weaker than observed. This latter error is also seen in the JJAS rainfall climatology (Fig. 1i and 1j). Even so, there is improvement in the CMIP5 MMM compared to the CMIP3 MMM, with a more realistic magnitude of rainfall between 10^{o}N-20^{o}N during July and August. Consistent with the results given in Figs. 1d and 1e, this improvement is related to the better representation of monsoon rainfall adjacent to the Western Ghats in CMIP5 compared to CMIP3. The annual cycle skill scores from all of the models are further evidence of improvement in the simulation of the annual cycle of rainfall in CMIP5 compared to CMIP3 (Fig. 4g). Notably, 6/10 and 13/20 of the largest skill scores are from CMIP5 models.

4.2 Monsoon Onset, Peak, Withdrawal, and Duration

The analysis of the annual cycle of the monsoon using pentad data is restricted to 21/25 CMIP5 models and 18/22 CMIP3 models due to limitations in the availability of high-frequency rainfall data. To facilitate the analysis, the climatological pentads of rainfall from the models have first been regridded to the GPCP grid. Our methodology closely follows that of Wang and LinHo (2002). At each gridpoint the pentad time series is smoothed with a five pentad running mean. The smoothing removes high-frequency fluctuations that arise due to the limited sample size, while retaining the climatological intraseasonal oscillation (LinHo and Wang 2002). The January mean rainfall is then removed from each pentad, resulting in the relative rainfall rate. Using GPCP data, an example of the relative rainfall rate for the Bay of Bengal is given in Fig. 5. At a given gridpoint, the boreal summer monsoon is taken to occur if the relative rainfall rate exceeds 5mm day^{-1} during May-September. Onset is defined as the first pentad at which this threshold is met or exceeded. The time of peak monsoon is the pentad at which the maximum relative rainfall rate occurs, and the withdrawal of the monsoon is the first pentad at which the relative rainfall rate falls below the onset criterion. The duration of the monsoon is defined as: (decay pentad) *minus* (onset pentad). Given that the monsoon is defined by a threshold criterion, the monsoon domain will be different for each of the models. Therefore, the MMM of the onset, peak, decay, and duration is calculated at gridpoints if half or more of the models have monsoon defined at that location. Skill is assessed using pattern correlation for gridpoints where both observations and models have monsoon defined.

Since the monsoon is defined by a threshold criterion, this approach is a severe test of a models ability to properly represent the observed amplitude and timing of the annual cycle of the monsoon. Thus, for a given model, absence of a signal relative to observations indicates that the model does not have the correct amplitude of the annual cycle, and this is a critical piece of information for modelers to consider during the course of model development.

The pentads of onset and the peak monsoon for the observations and models are given in Fig. 6. The observed pattern of onset, seen in Fig. 6a, is consistent with the analysis of Wang and LinHo (2002). Monsoon onset occurs first over Southeast Asia (Matusmoto 1997), and then subsequently over the South China Sea and to the southwest of India. Wu et al. (2012) have found that the development of the Asian summer monsoon onset vortex is a consequence of air-sea interaction over the Bay of Bengal. The onset progresses northward from these locations, subsequently engulfing India, southern China, Korea, Japan, and the western Pacific. The range of skill in simulating the pentad of monsoon onset is given by gfdl cm2.0 and inm-cm3.0 (Figs. 6b and 6c). The former model essentially has the progression correct, but the onset occurs later than observed over India. However, this model fails to define monsoon over northern China, Korea, and Japan, while it has overly extensive monsoon rainfall over the western/central Pacific Ocean. inm-cm3.0 also has a late onset over India, but the monsoon incorrectly progresses from north to south over China. The CMIP5 MMM has a larger pattern correlation with GPCP than the CMIP3 MMM (Figs. 6d and 6e, Table 2), indicating improvement in the ability to simulate the onset of the monsoon. This is seen as a more realistic onset time over Southeast Asia. However, for both MMM's, the onset still remains too late over India, and they overestimate the monsoon extension over the western/central Pacific Ocean. Contrary to the time-mean monsoon, individual models exceed the skill of the MMM.

Regarding the time of peak monsoon, the observations indicate that over the Arabian Sea and extending into India the peak time occurs progressively later, as it does from the southeast of Japan into eastern/central China (Fig. 6f). However, over southwestern China to Southeast Asia the peak monsoon rainfall occurs from north to south, indicating that the maximum rainfall occurs as the monsoon retreats. MIROC5 best represents this progression, though the time of the peak monsoon over India is too late (Fig. 6g), and the extent of the observed monsoon over the western Pacific is not simulated. echo-g qualitatively represents the northward progression of the peak pentad near India, though the actual timing is poorly represented there and over Southeast Asia (Fig. 6h). The CMIP5 MMM outperforms the CMIP3 MMM (Figs. 6i and 6j), though both are more uniform compared to observations in representing the time of the monsoon peak, and they lack the early peak near 90^{o}E over the Bay of Bengal. The spatial extent of the monsoon, in the CMIP5 MMM is more realistic than in the CMIP3 MMM, with the monsoon domain extending over northeast China. The spatial extent of the monsoon is discussed in more detail below.

The earliest withdrawal of the observed monsoon occurs over the West Pacific to the southeast of Japan, over China, and over the Arabian Sea, the periphery of the monsoon domain (Fig. 7a). Over East Asia the withdrawal progresses southward from northeast China, with the latest withdrawal occurring over Southeast Asia and the South China Sea. Over India, the results in Fig. 7a indicate that the GPCP data do not represent the smooth withdrawal of the monsoon from northwest India to southeast India (the reverse of the onset progression), as seen from the "Normal Date For Withdrawal of Southwest Monsoon" from the India Meteorological Department (http://www.imd.gov.in/section/nhac/dynamic/Monsoon_frame.htm). Our analysis indicates that CMAP data is more suitable for representing this aspect of the monsoon withdrawal. This is confirmed by comparing our CMAP results (not shown) with those from Wang and LinHo (2002, their Fig. 8). MIROC5 well represents the gross features of observed monsoon withdrawal, though it simulates a large land-sea contrast in the withdrawal time, and with the withdrawal occurring later than observed over India (Fig. 7b). echo-g also has a late withdrawal over India, with only a hint of evidence of north to south withdrawal over China due to its truncated monsoon domain (Fig. 7c). The CMIP5 MMM outperforms the CMIP3 MMM, though both MMM's are more zonal than observed in their north to south withdrawal (Figs. 7d and 7e). As for the onset phase, individual models outperform the MMM.

The observed duration of the monsoon is longest (~29-37 pentads) over Southeast Asia, and it becomes (more or less) progressively shorter with increasing radial distance over the surrounding monsoon domain (Fig. 7f). CNRM-CM5 well represents this gross structure (Fig. 7g), though the monsoon domain is not as contiguous as observed. A similar radial structure is seen in both MMM's (Figs. 7i and 7j), with CMIP5 better representing monsoon duration than CMIP3. Despite the late onset over India in the MMM's (Figs. 6d and 6e), the monsoon duration over India is overestimated by up to three pentads. These results suggest that over some regions the models have a monsoon seasonal cycle that is phase-delayed and/or longer in duration when compared to observations.

Figures 8a-8c show the skill of the models in simulating the pattern correlation relative to GPCP of the onset vs. the peak, withdrawal, and duration of the monsoon, respectively. The motivation is to evaluate which aspects of the annual cycle are best represented, and to test whether skill in simulating the onset, also translates into skill in representing the other stages in the annual cycle evolution of the monsoon. Figures 8a and 8b indicate that the skill in simulating the pattern of monsoon peak and monsoon withdrawal typically exceeds that of onset, but there is no statistical relationship in either peak or withdrawal skill relative to onset skill. However, the regression fits in Fig. 8c, significant at better than the 1% level, indicate that the pattern of the monsoon duration is better represented in models that have a better simulation of the onset pattern. In summary, the pattern correlation skill metrics indicate that the models are very diverse in their ability to simulate the monsoon annual cycle, with the CMIP5 MMM outperforming the CMIP3 MMM (Table 2). Biases in the annual cycle of SST, the spatial distribution of rainfall, and the vertical structure of the diabatic heating that are important for the circulation and moisture transports may all play a role in the errors in simulating the annual cycle evolution of the monsoon.

The hit rate and threat score are two categorical skill scores that are used to quantify the ability of the models to simulate the observed (GPCP) spatial domain of the monsoon. The skill analysis is performed over the region 40^{o}E-180^{o}E, 10^{o}S-50^{o}N (see Fig. 6). These skill scores are based on a 2x2 contingency table, where a = the number of grid points at which the model correctly represents the observed presence of monsoon, b = the number of gridpoints at which the model represents monsoon, but monsoon is not observed, c = the number of gridpoints at which the model represents the absence of monsoon, but monsoon is observed, and d = the number of grid points at which the model correctly represents the observed absence of monsoon. The hit rate is the fraction of model gridpoints that are correctly represented as observed monsoon and non-monsoon ([a + d]/[a + b + c + d]). The threat score, preferable when the quantity being forecast (the presence of the monsoon) occurs less frequently than the alternative (absence of the monsoon), "is the number of correct 'yes' forecasts divided by the total number of occasions on which that event was forecast and/or observed (a/[a + b + c]). It can be viewed as a hit rate for the quantity being forecast, after removing correct 'no' forecasts (d) from consideration" (Wilks 1995, p.240). A hit rate and threat score of 1.0 would indicate perfect agreement between model and observations. Figure 8d and Table 2 indicate that the CMIP5 MMM is more skillful than the CMIP3 MMM in representing the spatial extent of the monsoon, with individual models being more skillful than the MMM's. The low model skill relative to that between CMAP with GPCP confirms the results of Figs. 6 and 7 that improving the extent of the simulated monsoon domain is needed. Particularly problematic in the models is the lack of a monsoon extension over northeast China, Korea, and Japan, and the incorrect monsoon signal simulated over the central Pacific Ocean.

5 Interannual Variability

In this section we evaluate the interannual variability of (1) the ENSO-monsoon teleconnection, with emphasis on the rainfall response in South Asia to Niño3.4 SST anomalies, and (2) the response of rainfall and 850hPa wind in the East Asia region to the meridional gradient of the zonal wind anomalies at 850hPa.

5.1 Indian Summer Monsoon

The relationship between AIR and ENSO is one of the most studied teleconnections in climate science (see review article by Turner and Annamalai 2012). Annamalai et al. (2007) provided an analysis of the time-mean state and interannual-interdecadal variability of the Asian summer monsoon in the CMIP3 models. The complexities in representing (1) the spatial distribution of the time-mean monsoon rainfall, (2) the ENSO forcing from the tropical Pacific, and (3) the seasonality of the ENSO-monsoon relationship revealed that only four of the CMIP3 models were realistic in representing the interannual coupled atmosphere-ocean teleconnection between AIR and tropical SST.

Given in Fig. 9 and Table 3 is the lag 0 teleconnection between JJAS Niño3.4 SST anomalies and JJAS AIR anomalies. This provides a preliminary skill estimate of the models ability to represent the AIR-ENSO relationship. Over the period 1961-1999 the observations indicate the anti-correlation to be about -0.5. However, there is no expectation that the models should represent exactly this magnitude of anticorrelation, since their ENSO variability may be unrealistic, and/or their ENSO characteristics may be regime dependent with periods (decades or longer) when ENSO is stronger or weaker than presently observed (Wittenberg 2009). Therefore, the bounds of the observed interdecadal variability of the AIR-ENSO teleconnection are used to provide a constraint on evaluating model performance. The observed anticorrelation ranges from approximately -0.3 to -0.75 at interdecadal time scales, and rarely has it been statistically insignificant (Annamalai et al. 2007). Changes in the interdecadal strength of the observed anticorrelation are suggested to be related to changes in ENSO variance (Annamalai et al. 2012b) as well as changes to the lead-lag relationship between ENSO and June-July and August-September Indian monsoon rainfall (Boschat et al. 2012). Using these observed bounds, 11/25 (18/22) CMIP5 (CMIP3) models exhibit a statistically significant AIR-ENSO teleconnection.

The spatial pattern of the ENSO-forced rainfall anomalies is obtained from linear regression of JJAS Niño3.4 SST anomalies with JJAS rainfall anomalies (Fig. 10). The regressions are presented for one standard deviation of the Niño3.4 SST anomalies, and thus correspond to rainfall anomalies associated with El Niño. The high-resolution observations over India from Rajeevan et al. (2006) and the GPCP observations show similar characteristics for El Niño conditions. The largest rainfall decreases occur adjacent to the Western Ghats and near the foothills of the Himalayas, with a secondary rainfall deficit over central India, near 78^{o}E, 18^{o}N. Over northeastern India and near the Burmese coast, above-normal rainfall anomalies prevail, and are also seen in CMAP rainfall (not shown). With the strongest AIR-ENSO anticorrelation of the models analyzed (-0.76), the IPSL CM5A-MR simulation exhibits a stronger than observed deficit of rainfall over India, and enhanced rainfall near Burma (Fig. 10c). Additionally, this model has the largest pattern correlation, 0.64, of all models considered herein between the simulated and observed ENSO-forced rainfall anomalies. As seen in Fig. 10d, over India, the FGOALS-s2 model has a mixed rainfall signal, with a pattern correlation of only 0.10, and as such an insignificant AIR-ENSO teleconnection (0.11). Furthermore, this model has a strong rainfall enhancement over the Arabian Sea and the Bay of Bengal adjacent to India that is not seen in observations. An evaluation of the ENSO impact on the Asian monsoon in the FGOALS-s2 pre-industrial simulation is given by Wu and Zhou (2012). The CMIP5 MMM has a slightly larger pattern correlation with GPCP (0.62) than does the CMIP3 MMM (0.60), while individual models have larger pattern correlations than the MMM's (Table 3). Improvement in the CMIP5 MMM is also noted, since it also has larger rainfall anomalies than the CMIP3 MMM. However, in both cases the MMM anomalies are weaker than observed due to the wide-range of fidelity in simulating the precipitation teleconnections in the individual models.

The skill in representing the AIR-ENSO correlation vs. the pattern correlation of ENSO-forced rainfall anomalies with GPCP observations over 60^{o}E-100^{o}E, 0^{o}-30^{o}N is given in Fig. 9b. For the CMIP5 models there is a better than 1% statistically significant relationship between these skill metrics, indicating that the pattern of rainfall anomalies is better represented in models with a stronger anticorrelation between AIR and Niño3.4 SST anomalies. Conversely, as expected, models with a near-zero AIR-ENSO correlation have ENSO-forced rainfall anomaly pattern correlations that are not statistically significant. Interestingly, for AIR-ENSO correlations of about -0.3, the rainfall anomaly pattern correlations range from -0.14 to 0.53. This wide-range of skill in representing the rainfall anomaly pattern correlation can be due to many simulation features, such as the location and strength of the ENSO SST anomalies (Krishna Kumar et al. 2006), the spatio-temporal evolution of ENSO diabatic heating anomalies, and the proper seasonality of the AIR-ENSO relationship. As discussed in Annamalai et al. (2007), these interactions conspire to make simulation of the ENSO-monsoon teleconnection a challenge, with only four of the CMIP3 models representing the detailed aspects of this teleconnection. A more detailed diagnosis of the ENSO-monsoon teleconnection in the CMIP5 models is presented in Annamalai et al. (2012b). By examining all the ensemble members for the entire historical simulation period (~1850 to 2005), they note that the timing, amplitude, and spatial extent in the ENSO-monsoon relationship depends on the ability of the models' to capture the mean monsoon rainfall distribution and the ENSO-related SST and diabatic heating anomalies along the equatorial Pacific. They also note that incorrect simulation of regional SST anomalies over the tropical Indian Ocean and west Pacific sectors degrades the ENSO-monsoon association, even if the models capture ENSO realistically. This SST sensitivity is consistent with Lau and Nath (2012), who showed that during El Niño the tropical Pacific SST forcing and the warm SST anomalies in the Indian Ocean have opposing effects on the monsoon development. The role of SST errors over the Indian Ocean was investigated by Achuthavarier et al. (2012) using the NCEP Coupled Forecast System Model. They found that unrealistic early development of the Indian Ocean dipole prevents the Pacific ENSO signal from impacting the monsoon, and results in the inability of the model to generate the observed negative correlation of the ENSO-monsoon relationship. Thus, there are many critical factors for simulating a realistic ENSO-monsoon teleconnection, including indirect affects due to preceding boreal winter ENSO development (Wu et al. 2012).

5.2 East Asian Summer Monsoon

The East Asian summer monsoon (EASM) is a complicated region in that there are many competing mechanisms by which the monsoon is modulated. Influences from the Indian Ocean, ENSO, and from the eastern Pacific, plus local air-sea interactions over the South China Sea and interaction of tropical and subtropical circulation systems have been documented (Zhou et al. 2009b; Zhou et al. 2011). Thus, there are many observational metrics to assess model performance (Zhou and Li 2002; Chen et al. 2010; Boo et al. 2011), and a plethora of indexes for measuring the strength of the EASM. As discussed in Wang et al. (2008) the indexes fall broadly into five categories related to (1) East-West thermal contrast, (2) North-South thermal contrast, (3) wind shear vorticity, (4) southwest monsoon, and (5) South China Sea. In an effort to provide a unified approach to measuring the strength of the East Asian summer monsoon, Wang et al. (2008) have performed a multivariate Empirical Orthogonal Function (EOF) analysis using precipitation, sea-level pressure, and the zonal and meridional winds at 850hPa and

200hPa using JJA anomalies over the domain 100°E-140°E, 0°-50°N for 1979-2006. The leading mode, which is not related to the developing phase of ENSO, is characterized by enhanced precipitation along the East Asian subtropical front associated with interannual variations of the Meiyu/Baiu/Changma rainband. These authors found that the principal component (PC) of this leading mode had a correlation of -0.97 with JJA anomalies of the zonal wind shear index of Wang and Fan (1999), the strongest correlation among the 25 East Asian monsoon indexes considered in their paper. Thus, as a simple East Asian summer monsoon index for validating the CMIP5 and CMIP3 models we adopt the negative of the Wang and Fan (1999) zonal wind shear index:

WFN = (U_{850}; 110°E-140°E, 22.5°N-32.5°N) *minus* (U_{850}; 90°E-130°E, 5°N-15°N)

Figure 11a shows the regression of the WFN from JRA25 reanalysis with JJA anomalies of GPCP rainfall and JRA25 850hPa wind for 1979-2007. These rainfall and wind anomalies are consistent with the multivariate EOF anomalies presented in Figures 2a and 5a of Wang et al. (2008). Furthermore, pattern correlations of these anomalies with those derived from CMAP and NCEP/NCAR reanalysis are 0.99 and 0.96, respectively (Table 3), indicating that these features are robust characteristics of East Asian summer monsoon variability.

For both CMIP5 and CMIP3, the MMM's are equally adept at representing the wind anomalies (Figs. 11b and 11c), with CMIP5 being superior to CMIP3 in representing the pattern of rainfall anomalies, especially the deficit rainfall adjacent to the west coast of the Philippines. The MMM are poor in representing the rainfall maxima that extends from central China to Southwest Japan. Additionally, the MMM rainfall anomalies are smaller than observed or simulated by individual models; a feature also noted for the ENSO forced rainfall anomalies over the Indian sector (Figs. 10e and 10f). Figures 11d and 11e show the anomalies for models that have the largest and smallest 850hPa wind anomaly pattern correlations compared to JRA25. In gfdl cm2.0 the 850hPa pattern correlation is nearly identical to that of the MMM, while the pattern correlation of the precipitation anomalies is smaller. iap fgoals-g1.0 has enhanced rainfall near 30°N with below normal rainfall to the south, though the details of the observed spatial pattern are not well represented. Furthermore, the relationship of the enhanced rainfall to the western Pacific subtropical high and anti-cyclonic 850hPa wind anomalies are not properly represented. Rather, the enhanced rainfall is associated with strong cyclonic wind anomalies near 40°N, with a possible contribution of moisture from the westerly monsoon flow over Southeast Asia. This bias is related to the weak western Pacific summer monsoon and deficient rainfall surrounding the Philippines in the atmospheric model component of iap fgoals-g1.0 (Liu et al. 2011). HadGEM2-ES has the largest rainfall pattern correlation of the models analyzed, with an excellent representation of the rainfall minima adjacent to the west coast of the Philippines, and the maxima over southeast China and southwest Japan (Fig. 11f). INM CM4 has a weak signal in the 850hPa wind anomalies, indicating that the simulated subtropical high is not modulating the flow as strongly as observed. As a consequence the rainfall is not modulated as observed.

The skill assessment of the ability of the models to simulate East Asian monsoon patterns of rainfall and 850hPa wind anomalies over 100°E-140°E, 0°-50°N is presented in Fig. 12. For both CMIP5 and CMIP3 the 850hPa wind anomalies are better simulated than the rainfall anomalies (Fig. 12a), consistent with the CMIP3 analysis of Boo et al. (2011). The CMIP5 MMM rainfall anomalies and 850hPa wind anomalies have larger pattern correlations relative to those from the CMIP3 MMM. For both sets of models there is a better than 5% significant relationship of a correspondence between the quality of the 850hPa wind anomalies and the rainfall anomalies. As seen in Figs. 12b and 12c for 850hPa wind and rainfall, respectively, there is no relationship between the quality of the interannual variability and the climatology over the East Asian region. Interestingly, the interannual variability of the 850hPa wind anomalies is better represented than the wind climatology for all but 3 models (Fig. 12b), while for the majority of models the rainfall climatology is better represented than the interannual variability (Fig. 12c). A reasonable representation of climate mean monsoon rain band over East Asia relies heavily on convection parameterization (Chen et al. 2010).

The analysis of the interannual variability of the Asian summer monsoon indicates that there is a wide-range of performance among the models, with substantial scope for model improvement in the simulation of the rainfall anomalies. A summary of the ability of the models to simulate the interannual variability of rainfall for the Indian summer monsoon and the East Asian monsoon is given in Fig. 12d. Relative to GPCP rainfall, it shows the pattern correlations of the interannual rainfall anomalies over the East Asian Summer Monsoon domain (also see Figs. 11, 12a, and 12c) are better simulated than the pattern correlations of the interannual rainfall anomalies over the Indian Monsoon domain (also see Figs. 9b and 10). The lack of a statistical relationship between the interannual variations over these regions confirms that the controlling mechanisms are distinct for the two regions, and that progress in modeling monsoon interannual variability requires fidelity in representing a wide variety of processes.

6 Boreal Summer Intraseasonal Variability

BSISV of the monsoon is the dominant modulator of convection over the Asian domain, and it has been shown to contribute to interannual variability of the monsoon (Sperber et al. 2000). Where the environment is favorable for convection over a broad region, embedded features, such as tropical depressions and typhoons, are important contributors to total seasonal rainfall. On modeling intraseasonal time scales, Sperber and Annamalai (2008) found that only 2 of 17 CMIP3 and CMIP2+ models analyzed could represent the life cycle of the leading mode of 30-50 day BSISV. Lin et al. (2008) found that the 12-24 day mode was better represented than the BSISV in CMIP3. Even so, the BSISV simulation in the CMIP3 models was a marked improvement compared to the previous generation of models (Waliser et al. 2003).

Following the analysis of the CMIP3 models by Sperber and Annamalai (2008), the BSISV is characterized by 20-100 day bandpass filtered variance, and by evaluation of the models ability to simulate the spatio-temporal evolution of the leading Cyclostationary EOF (CsEOF) of filtered OLR that was described in Annamalai and Sperber (2005). Due to limited availability of daily data, 16 CMIP5 models and 15 CMIP3 are analyzed herein. Given the CMIP3 analysis of Sperber and Annamalai (2008), we predominantly concentrate on the performance of the CMIP5 models herein.

The 20-100 day bandpass filtered variance from observations and models is shown in Figs. 13a-f. The MPI ESM-LR model (Fig. 13b), with a pattern correlation of 0.87 relative to the AVHRR OLR (Fig. 13a), has the best representation of the variance pattern of the models considered (Table 3). Consistent with previous MPI models, it has skillful performance for this baseline intraseasonal diagnostic. Importantly, the CMIP5 model version has a more realistic amplitude of OLR variance, which in previous versions was substantially overestimated. Additional improvement is with respect to the partitioning of variance between the continental longitudes (~15^{o}N-20^{o}N) and the smaller values over the near-equatorial Indian Ocean. Of the CMIP5 models, the MIROC-ESM model has the smallest pattern correlation with observations, 0.55. It exhibits pockets of strong intraseasonal variability with a pronounced variance minimum near 10^{o}N over the Indian Ocean that unrealistically separates the variance maxima over the continental latitudes (~20^{o}N) and the near-equatorial region (Fig. 13c). The MIROC5 model, which will be discussed in more detail below, has intermediate skill, with a pattern correlation of 0.81 (Fig. 13d). The CMIP5 MMM, Fig. 13e, has larger skill than the best model and the CMIP3 MMM (Fig. 13f and Table 3). Furthermore, the magnitude of the intraseasonal variance in the CMIP5 MMM is more realistic than that from the CMIP3 MMM.

The observed BSISV life cycle is presented in Fig. 14. The 20-100 day bandpass filtered OLR anomalies for JJAS 1979-2007 are projected on to the Day 0 CsEOF pattern of Annamalai and Sperber (2005). Using lag regression, the resulting PC (referred to as PC-4 in Sperber and Annamalai 2008) is regressed back onto the filtered OLR to obtain the spatio-temporal evolution of the BSISV. As in Sperber and Annamalai (2008), projection of the model 20-100 day bandpass filtered OLR onto the observed Day 0 CsEOF pattern ensures that the models are analyzed using a uniform approach, which addresses the question: How well do the models simulate the observed BSISV? The observed results in Fig. 14 are plotted where the regressions are statistically significant, assuming every pentad is independent. As seen in Fig. 14a and 14b, the enhanced convection first begins near the east coast of equatorial Africa, and extends into the western Indian Ocean. Over the central and eastern Indian Ocean suppressed convection dominates. From Day -5 through Day 0, Figs. 14c and 14d, the enhanced convection over the Indian Ocean amplifies and extends eastward to the Maritime Continent, while a tilted band of suppressed convection dominates to the north, extending from the Arabian Sea to the western Pacific. By Day 5, Fig. 14e, the enhanced convection bifurcates near the equator over the Indian Ocean, with the strongest convective anomalies extending southeastward from the Arabian Sea and India to New Guinea. At this time the suppressed convection dominates over the western Pacific near 15^{o}N. By Day 10, Fig. 14f, the northwest to southeast tilted region of enhanced convection extends from the Arabian Sea to the equatorial central Pacific. This structure arises due to northward propagation of convective anomalies in the vicinity of the Indian longitudes, as the equatorial convective anomalies propagate eastward from the Indian Ocean to the Maritime Continent/west Pacific. The tilt arises due to the favorable vertical wind shear and the shedding of Rossby waves over this domain during boreal summer (Lau and Peng 1990; Wang and Xie 1997; Annamalai and Sperber 2005). Over the west Pacific near 15^{o}N the suppressed convection weakens and diminishes in extent. With the development of suppressed convection over the equatorial Indian Ocean there is a quadrapole pattern of convective anomalies that persists through Day 15, Fig. 14g, that then weakens by Day

20, Fig. 14h. The tilted band of enhanced convection weakens, and the suppressed convection over the Indian Ocean begins to dominate. These stages in the BSISV lifecycle, obtained via regression (the approach needed to analyze the models), compare well with the evolution of the CsEOF's of Annamalai and Sperber (2005, see their Fig. 2), with which they have pattern correlations of 0.83 or larger.

The skill of the models in simulating the observed 20-100 bandpass filtered variance and the BSISV lifecycle is presented in Fig. 15. The filtered variance accounts for both standing and propagating components while the BSISV is the leading propagating mode. The skill for the filtered variance is based on the pattern correlation of the model with observations. The model skill of the BSISV life cycle is the space-time pattern correlation of the best matching lag regressions to the Day -15, Day -10, Day -5, Day 0, Day 5, Day 10, Day 15, and Day 20 patterns from the observed BSISV CsEOF (Annamalai and Sperber 2005). Data at all gridpoints over the region 40^{o}E-180^{o}E, 30^{o}S-30^{o}N are used for the calculation of the skill scores. The results indicate that at better than the 1% significance level there is a statistically significant relationship between the filtered variance pattern and the BSISV life cycle for both the CMIP5 and CMIP3 models. This suggests that the location and strength of the filtered variance maxima are largely determined by the propagating BSISV. The skill of the CMIP5 MMM is slightly larger than the CMIP3 MMM, and the filtered variance pattern tends to be better simulated than the BSISV life cycle.

To facilitate the evaluation of the BSISV life cycle, animations of the BSISV life cycle from the CMIP5 models and observations can be found at: http://www-pcmdi.llnl.gov/projects/ken/cmip5_bsisv/index.html, while the animations from the CMIP3 and CMIP2+ models analyzed by Sperber and Annamalai (2008) can be found at: http://www-pcmdi.llnl.gov/projects/ken/. In Sperber and Annamalai (2008), only two models showed appreciable skill at representing the BSISV life cycle, including the northwest to southeast tilted band of enhanced convection. Both coupled models were Max Planck Institute derived models that used the same atmospheric model (European Centre Hamburg-4; ECHAM4). In CMIP5, the MIROC5 model has the largest space-time correlation of the BSISV life cycle with observations (0.69). As seen in Fig. 16, the BSISV life cycle of the MIROC5 model exhibits many of the observed features seen in Fig. 14, especially the strongly suppressed convection over the Indian Ocean on Day -15 (Fig. 16a). It also represents well the amplification and eastward propagation of enhanced convection over the equatorial Indian Ocean and the tilted band of suppressed convection to the north from Day -10 through Day 0 (Figs. 16b-16d). The bifurcation of enhanced convection over the central/eastern Indian Ocean is seen on Day 5 (Fig. 16e), though the strongest anomalies are incorrectly located south of the equator. Although present from Day 10 through Day 20 (Figs. 16f-16h), the tilted region of enhanced convection is not as spatially contiguous as observed, and the anomalies are weaker than observed. Another shortcoming of the simulation is that the convective anomalies over the western Pacific are not as strong as observed. Even so, the simulation of the BSISV life cycle by MIROC5 is an important step forward, since an atmospheric model with a different formulation from ECHAM4 shows the capability to simulate important aspects of the BSISV life cycle, especially the northwest to southeast tilted band of enhanced convection. Despite using the same convection scheme as ECHAM4, the more recent MPI derived models, MPI-ESM-LR and echam5/mpi-om, do not properly represent the tilted band of convection. Subsequent to ECHAM4, replacement and/or changes to the grid-scale condensation scheme and radiation schemes have occurred in the MPI-based models. Since the MJO has been shown to be sensitive to cloud-radiation interaction (Ma and Kuang 2011), it has been suggested that these modifications may account for the reduced skill in simulating MJO in these more recent MPI models (D. Kim, personal communication, 2012).

MRI-CGCM3, and to a lesser extent GFDL-ESM2G, also show a tilted region of convection, but the extension into the western equatorial Pacific occurs after the northward propagation reaches 20^{o}N over India and the Bay of Bengal, whereas in observations the eastward extension and northward propagation occur in tandem. Mizuta et al. (2012) suggest that the improvement of the BSISV in the MRI model is due to modification of the convection scheme, which allows for higher levels of convective available potential energy to build-up before the instability is released. Rectifying model errors, including those related to SST and tropospheric temperature over the Indian Ocean, may result in a more realistic representation of the northward propagation of the BSISV, and consequently the interannual variability of the Indian monsoon (Joseph et al. 2012). Excepting those CMIP5 models that have westward propagation over the equatorial Indian Ocean, FGOALS-s2 and NorESM1-M, the majority of models have difficulty in getting the enhanced equatorial convection to propagate into the western Pacific, consistent with the CMIP3 results of Sperber and Annamalai (2008).

Given the wide-range of model performance in representing the BSISV life cycle, it was surprising to find that the CMIP5 and CMIP3 MMM's were more skillful than the individual models. The life cycle of the CMIP5 MMM is shown in Fig. 17. In an effort to show statistical significance, the averages at each gridpoint were calculated if more than half of the models had a statistically significant convective anomaly (irrespective of sign) at that time lag. As such, the anomalies are slightly larger than those from the "true" MMM used for the skill score calculation in Fig. 15, in which the arithmetic mean of all models was taken at each gridpoint, at each time lag. With the exception of representing the tilted band of suppressed convection that is observed on Day -10 (compare Fig. 17b with Fig. 14b), the CMIP5 MMM represents the major aspects of the life cycle of the BSISV. Furthermore, compared to MIROC5, the CMIP5 MMM better represents the spatial extent and magnitude of the convective anomalies over the western Pacific (compare Figs. 17c-17h with Figs. 16c-16h). These astounding results suggest the potential for making skillful multi-model forecasts of the BSISV.

Future work on the BSISV will include a more detailed evaluation to assess if the physical processes involved are consistent between the observations and the most skillful models, to evaluate the impact of climate change on the BSISV, and explore the usefulness of the MMM in this regard.

7 Discussion and Conclusions

The CLIVAR Asian-Australian Monsoon Panel Diagnostics Task Team selected the diagnostics presented herein. These diagnostics provide a broad overview of the state-of-the-art in simulating boreal summer Asian monsoon as of 2011. The most important take away message is that in terms of the MMM, the CMIP5 models outperform the CMIP3 models for all of the diagnostics. While the CMIP5 MMM gains in terms of the skill scores are incremental, additional supporting evidence is noted, such as the improved amplitude of precipitation in the CMIP5 MMM relative to the CMIP3 MMM. Even so, there are systematic errors that are consistent between the two vintages of models. For example, the time mean rainfall error has a consistent pattern between CMIP5 and CMIP3 (Figs. 1i and 1j), though the amplitude of the error is smaller in CMIP5 relative to CMIP3. Part of the error reduction is the better simulation of the precipitation maxima in the vicinity of steep orography. Other systematic errors that are common to both sets of models include (1) late monsoon onset over India and poor representation of the annual cycle of the Indian monsoon and oceanic rainfall bands, (2) the monsoon domain not extending far enough north over China, Korea, and Japan, and (3) the monsoon domain extending too far to the east over the Pacific Ocean (Figs. 6a-6e). For the time mean state and the interannual variability over East Asia, the 850hPa wind is better simulated than the precipitation (Figs. 3 and 12a). On intraseasonal time scales, changes to convective parameterizations have contributed to new models representing important aspects of the BSISV (Mizuta et al. 2012). The MIROC5 model (Watanabe et al. 2010) provides a credible simulation of the leading mode of the BSISV (Fig. 16). This is an important advance, since heretofore only ECHAM4-based models showed similar capability (Sperber and Annamalai 2008). Despite the poor representation of the BSISV in most of the models, especially seen in the animations, the CMIP5 MMM outperforms the individual models (Figs. 15 and 17). This suggests that a multi-model approach to forecasting the BSISV might be fruitful.

Given that the aim of this paper has been a comparison of CMIP5 relative to CMIP3, we have taken the basic approach of generating MMMs using all models (with the exception of the monsoon domain extent [Fig. 6] and the BSISV [Fig. 17]), even though in some cases individual institutions have made multiple submissions with slightly different model versions. More exhaustive approaches to assessing model independence and weighting can be applied (Mason and Knutti 2011), but this is beyond the scope of this overview. Furthermore, skill for some phenomena, such as the relationship between AIR and ENSO and the impact of climate change on this teleconnection, requires the joint assessment of multiple facets of model performance, including the climatology of rainfall over India, and the fidelity with which ENSO is simulated (Annamalai et al. 2007, 2012b). However, for assessing larger scale impacts, incorporating model quality information using parametric and non-parametric weighting approaches based on mean state, annual cycle, and El Niño variability has been shown to NOT affect conclusions in climate detection and attribution studies (Santer et al. 2009). Thus, there is no unique best approach to generating MMMs. We suggest that the skill scores presented herein be used as a starting point for selecting subsets of models for more in-depth analysis of boreal summer Asian monsoon phenomena. Furthermore, given the overlap of skill between individual CMIP5 and CMIP3 models, it is suggested that the CMIP5 and CMIP3 models be viewed as a joint resource for investigating processes and climate change impacts, rather than dismissing the CMIP3 models simply because they predate the CMIP5 models.

In the figures we have presented the range of model performance for each of the diagnostics. In many instances, only fractions of a percent separate one model from the next in terms of skill. In an effort to look for consistency in skill, in Tables 2 and 3 we have highlighted the five models that have the largest skill scores for each diagnostic. This approach reveals numerous common features: (1) NorESM1-M and CCSM4, which use the same atmospheric model, consistently finish in the top five in 9/14 and 7/12 categories, respectively. Both models are top five finishers in simulating the rainfall climatology, and most aspects of the climatological annual cycle of pentad rainfall. The former model also performs consistently well in representing the interannual variability; (2) the MIROC5 and MIROC4h models have complimentary skill in representing the climatological annual cycle of pentad rainfall; (3) the IPSL-CM5a-LR and IPSL-CM5a-MR models are top five performers in representing the interannual variability of the Indian monsoon; (4) several of the GFDL models are top five performers in representing the climatology and the interannual variability of the 850hPa wind; and (5) the ECHAM based models tend to have large skill scores on intraseasonal time scales. Given our focus on a limited set of boreal summer Asian monsoon diagnostics, we emphasize that the discussion of skill given in this paper is not necessarily representative of overall model performance.

The diagnostics and associated skill estimates presented are not exhaustive in scope, and given the regional complexity of the monsoon (Zhou et al. 2011), there is ample scope for additional analysis of other aspects of monsoon variability and change (e.g. Zhou et al. 2009c; Zhou and Zou 2010; Boo et al. 2011, Li and Zhou 2011; Meehl et al. 2012). Furthermore, it is important to more fully diagnose the multitude of processes and interactions that are associated with the different aspects of monsoon variability. Examples of more in-depth questions to address include (1) evaluating the partitioning of rainfall into convective vs. large-scale components, (2) assessing how well the models represent the main rain-bearing synoptic systems, and (3) investigating if there is a relationship between the ability of the models to represent the BSISV and simulate the onset of the monsoon correctly, especially over India where onset is systematically too late. Through such diagnoses, we will gain an improved understanding of model processes and scale interactions. We may also gain confidence that subsets of the models are more reliable for investigating the impact of climate change on the monsoon (e.g. Annamalai et al. 2007, 2012b). The analysis presented here, and for multi-model seasonal forecasts of Indian summer monsoon (Rajeevan et al. 2012), highlight the beneficial impact that parameterization development and increased horizontal resolution have had on the simulation of boreal summer monsoon climate and variability.

Acknowledgements We thank the CLIVAR AAMP and other invited experts for helpful comments and encouragement during the course of this work. We acknowledge the World Climate Research Programme's Working Group on Coupled Modelling, which is responsible for CMIP, and we thank the climate modeling groups (listed in Table 1 of this paper) for producing and making available their model output. For CMIP the U.S. Department of Energy's Program for Climate Model Diagnosis and Intercomparison provides coordinating support and led development of software infrastructure in partnership with the Global Organization for Earth System Science Portals. K. R. Sperber was supported by the Office of Science (BER), U.S. Department of Energy through Lawrence Livermore National Laboratory contract DE-AC52-07NA27344. H. Annamalai was supported by the Office of Science (BER) U.S. Department of Energy, Grant DEFG02-07ER6445, and also by three institutional grants (JAMSTEC, NOAA and

NASA) of the International Pacific Research Center. In-Sik Kang was supported by the National Research Foundation of Korea (NRF-2009-C1AAA001-2009-0093042). Aurel Moise was supported by the Australian Climate Change Science Program, funded jointly by the Department of Climate Change and Energy Efficiency, the Bureau of Meteorology and CSIRO. A. G. Turner is supported by a NERC Fellowship reference number NE/H015655/1. B. Wang was supported by US NSF award #AGS-1005599.

References

Achuthavarier D, Krishnamurty V, Kirtman BP, Huang B (2012) Role of the Indian Ocean in the ENSO–Indian Summer Monsoon Teleconnection in the NCEP Climate Forecast System. J Clim 25:2490-2508. doi:10.1175/JCLI-D-11-00111.1

Annamalai H, Hafner J, Sooraj KP, Pillai P (2012a) Global warming shifts monsoon circulation, drying South Asia. J Clim (in press)

Annamalai H, Mehari M, Sperber KR (2012b) A recipe for ENSO-monsoon diagnostics in CMIP5 models. J Clim (in preparation)

Annamalai H, Hamilton K, Sperber KR (2007) The south Asian summer monsoon and its relationship to ENSO in the IPCC AR4 simulations. J Clim 20:1071-1092. doi: 10.1175/JCLI4035.1

Annamalai H, Sperber KR (2005) Regional heat sources and the active and break phases of boreal summer intraseasonal (30-50 day) variability. J Atmos Sci 62:2726-2748

Annamalai H, Slingo JM, Sperber KR, Hodges K (1999) The mean evolution and variability of the Asian summer monsoon: comparison of ECMWF and NCEP-NCAR reanalyses. Mon Weather Rev 127:1157-1186

Arkin PA, Ardanuy PE (1989) Estimating climatic-scale precipitation from space: a review. J Clim 2:1229–1238

Blanford HF (1884) On the connection of the Himalaya snowfall with dry winds and seasons of drought in India. Proc Roy Soc London, 37:3-22

Bollasina M, Nigam S (2009) Indian Ocean SST, evaporation, and precipitation during the South Asian summer monsoon in IPCC AR4 coupled simulations. Clim Dyn 33:1017-1032. doi:10.1007/s00382-008-0477-4

Boo K-O, Martin G, Sellar A, Senior C, Byun Y-H (2011) Evaluating the East Asian monsoon simulation in climate models. J Geophys Res 116:D01109, doi:10.1029/2010JD014737

Boschat G, Terray P, Masson S (2012) Robustness of SST teleconnections and precursory patterns associated with the Indian summer monsoon. Clim Dyn 38:2143-2165. doi:10.1007/s00382-011-1100-7

Charney J, Shukla J (1981) Predictability of monsoons. In: Lighthill J, Pearce RP (eds) Monsoon Dynamics. Cambridge University Press, Cambridge, pp 99-109

Chen H, Zhou T, Neale RB, Wu X, Zhang GJ (2010) Performance of the new NCAR CAM3.5 in East Asian summer monsoon simulations: sensitivity to modifications of the convection scheme. J Clim 23:3657-3675

Findlater, J (1970) A major low-level air current near the Indian ocean during northern summer: interhemispheric transport of air in the lower troposphere over the western Indian ocean. Q J R Meteorol Soc 96:551-554

Gadgil S, Sajani S (1998) Monsoon precipitation in the AMIP runs. Clim Dyn 14:659-689

Gill AE (1980) Some simple solutions for heat-induced tropical circulation. Q J R Meteorol Soc 106:447-462

Hoskins BJ, Rodwell MJ (1995) A model of the Asian summer monsoon. Part 1: the global scale. J Atmos Sci 52:1329-1340

Huffman GJ, Adler RF, Morrissey MM, Bolvin DT, Curtis S, Joyce R, McGavock B, Susskind J (2001) Global precipitation at one-degree daily resolution from multisatellite observations. J Hydrometeorol 2:36–50

Joseph S, Sahai AK, Goswami BN, Terray P, Masson S, Luo J-J (2012) Possible role of warm SST bias in the simulation of boreal summer monsoon in SINTEX-F2 coupled model. Clim Dyn 38:1561-1567. doi:10.1007/s00382-011-1264-1

Kalnay E, Kanamitsu M, Kistler R, Collins W, Deaven D, Gandin L, Iredell M, Saha S, White G, Woollen J, Zhu Y, Chelliah M Ebisuzaki W, Higgins W, Janowiak J, Mo KC, Ropelweski C, Wang J, Leetma A, Reynolds R, Jenne R, Joseph D (1996) The NCEP/NCAR 40-year reanalysis project. Bull Amer Meteorol Soc 77:437–471

Krishna Kumar K, Rajagopalan, Hoerling M, Bates G, Cane M (2006) Unraveling the mystery of Indian monsoon failure during El Nino. Science 314:115-119. doi:10.1126science.1131152

Lau KM, Kim K-M (2010) Pakistan flood and Russian heatwave: Teleconnection of hydrometeorologic extremes. J Hydrometeorol 13:392–403

Lau KM, Peng L (1990) Origin of low-frequency (intraseasonal) oscillations in the tropical atmosphere. Part III: monsoon dynamics. J Atmos Sci 47:1443-1462

Lau N-C, Nath MJ (2012) A model study of the air-sea interaction associated with the climatological aspects of interannual variability of the South Asian summer monsoon development. J Clim 25:839-857. doi:10.1175/JCLI-D-11-00035.1

Li B, Zhou T (2011) ENSO-related Principal Interannual Variability Modes of Early and Late Summer Rainfall over East Asia in SST-driven AGCM Simulations, J Geophys Res 116:D14118. doi:10.1029/2011JD015691

Li C, Yanai M (1996) The onset and Interannual variability of the Asian summer monsoon in relation to land sea thermal contrast. J Clim 9:358-375

Liebmann B, Smith CA (1996) Description of a complete (interpolated) OLR dataset. Bull Amer Meteorol Soc 77:1275–1277

Lin J-L, Weickmann KM, Kiladis GN, Mapes BE, Schubert SD, Suarez MJ, Bacmeister JT, Lee M-I (2008) Subseasonal variability associated with the Asian Summer monsoon simulated by 14 IPCC AR4 coupled GCMs. J Clim 21:4541-4567. doi:10.1175/2008JCLI1816.1

Liu X, Zhou T, Zhang L, Zou L, Wu B, Li Z (2011) The western North Pacific summer monsoon simulated by GAMIL1.0: Influence of the parameterization of wind gustiness. Chinese J Atmos Sci 35:871-884 (In Chinese)

LinHo, Wang B (2002) The time-space structure of the Asian-Pacific summer monsoon: A fast annual cycle view. J Clim 15:3206–3221

Mason D, Knutti R (2011) Climate model geneology. Geophys Res Lett 38: L08703. doi:10.1029/2011GL046864

Ma D, Kuang Z (2011) Modulation of radiative heating by the Madden-Julian oscillation and convectively coupled Kelvin waves as observed by CloudSat. Geophs Res Lett 38:L21813. doi: 10.1029/2011GL049734

Matsumoto J (1997) Seasonal transition of summer rainy season over Indochina and adjacent monsoon regions. Adv Atmos Sci 14:231-245

Meehl, GA, Covey, C, Delworth, T, Latif, M, McAvaney, B, Mitchell, JFB, Stouffer, RJ, Taylor, KE (2007) The WCRP CMIP3 multi-model dataset: A new era in climate change research. Bull Amer Meteorol Soc 88:1383-1394

Meehl GA, Arblaster JM, Caron JM, Annamalai H, Jochum M, Chakraborty A, Murtugudde R (2012) Monsoon regimes and processes in CCSM4, part 1: the Asian-Australian monsoon. J Clim 25:2583-2608. doi:10.1175/JCLI-D-11-00184.1

Mizuta R, Yoshimura H, Murakami H, Matsueda M, Endo H, Ose T, Kamiguchi K, Hosaka M, Sugi M, Yukimoto S, Kusunoki S, Kitoh A (2012) Climate simulations using MRI-AGCM3.2 with 20-km grid. J Meteorol Soc Japan 90A:233-258. doi:10.2151/jmsj.2012-A12

Nakazawa T (1986) Intraseasonal variations of OLR in the tropics during the FGGE year. J Meteorol Soc Japan 64:17-34

Onogi K, Tsutsui J, Koide H, Sakamoto M, Kobayashi S, Hatsushika H, Matsumoto T, Yamazaki N, Kamahori H, Takahashi K, Kadokura S, Wada K, Kato K, Oyama R, Ose T, Mannoji N, Taira R (2007) The JRA-25 Reanalysis. J Meteorol Soc Japan 85:369-432

Pearce RP, Mohanty UC (1984) Onsets of the Asian summer monsoon 1979-82. J Atmos Sci 41:1610-1639

Prasanna V, Annamalai H (2012) Moist dynamics of extended monsoon breaks over South Asia. J Clim 25:3810-3831. doi:10.1175/JCLI-D-11-00459.1

Rajeevan M, Najundiah RS (2009) Coupled model simulations of twentieth century climate of the Indian summer monsoon. In: Mukunda N (ed) Current Trends in Science, Indian Academy of Sciences, pp 537-567 (http://www.ias.ac.in/academy/pjubilee/book.html)

Rajeevan M, Bhate J, Kale JD, Lal B (2006) High resolution daily gridded rainfall data for the Indian region: analysis of break and active monsoon spells. Current Science 91:296-306

Rajeevan M, Unnikrishnan CK, Preethi B (2012) Evaluation of the ENSEMBLES multi-model seasonal forecasts of Indian summer monsoon variability. Clim Dyn 38:2257-2274. doi:10.1007/s00382-011-1061-x

Santer BD, Taylor KE, Gleckler PJ, Bonfils C, Barnett TP, Pierce DW, Wigley TML, Mears C, Wentz FJ, Bruggemann W, Gillet NP, Klein SA, Solomon S, Stott PA, Wehner MF (2009) Incorporating model quality information in climate change detection and attribution. Proc Nat Acad Sci 106:14778-14783

Slingo J., Annamalai H (2000) 1997: The El Niño of the Century and the Response of the Indian Summer Monsoon. Mon Weather Rev 128: 1778-1797

Sperber KR, Annamamlai H (2008) Coupled model simulations of boreal summer intraseasonal (30-50 day) variability, part 1: systematic errors and caution on use of metrics. Clim Dyn 31:345-372. doi:10.1007/s00382-008-0367-9

Sperber KR, Palmer TN (1996) Interannual tropical rainfall variability in general circulation model simulations associated with the atmospheric model intercomparison project. J Clim 9:2727–2750

Sperber KR, Slingo JM, Annamalai H (2000) predictability and the relationship between subseasonal and interannual variability during the Asian summer monsoon. Q J R Meteorol Soc 126:2545-2574

Taylor KE, Stouffer RJ, Meehl GA (2012) An Overview of CMIP5 and the experiment design." Bull Amer Meteorol Soc 93:485-498. doi:10.1175/BAMS-D-11-00094.1

Turner AG, Annamalai H (2012) Climate change and the south Asian summer monsoon. Nature Clim Change 2:1-9. doi:10.1038/NCLIMATE1495

Turner AG, Sperber KR, Slingo J, Meehl G, Mechoso CR, Kimoto M, Giannini A (2011) Modelling monsoons: understanding and predicting current and future behavior. In: Chang C-P, Ding Y, Lau N-C, Johnson RH, Wang B, Yasunari T (eds) The Global Monsoon System: Research and Forecast, 2nd edn. World Scientific Publishing Co., Singapore, pp 421-454

Uppala SM, Kallberg PW, Simmons AJ, Andrae U, Bechtold VD, Fiorino M, Gibson JK, Haseler J, Hernandez A, Kelly GA, Li X, Onogi K, Saarinen S, Sokka N, Allan R. P, Andersson E, Arpe K, Balmaseda MA, Beljaars ACM, Van De Berg L, Bidlot J, Bormann N, Caires S, Chevallier F, Dethof A, Dragosavac M, Fisher M, Fuentes M, Hagemann S, Holm E, Hoskins BJ, Isaksen L, Janssen PAEM, Jenne R, McNally AP, Mahfouf JF, Morcrette JJ, Rayner NA, Saunders RW, Simon P, Sterl A, Trenberth KE, Untch A, Vasiljevic D, Viterbo P, Woollen J (2005) The ERA-40 re-analysis. Q J R Meteorol Soc 131:2961-3012

Waliser DE, Jin K, Kang I-S, Stern WF, Schubert SD, Wu MLC, Lau K-M, Lee M-I, Krishnamurty V, Kitoh A, Meehl GA, Galin VY, Satyan V, Mandke SK, Wu G, Liu Y, Park C-K (2003) AGCM simulations of intraseasonal variability associated with the Asian summer monsoon. Clim Dyn 21:423–446. doi:10.1007/s00382-003-0337-1

Walker GT (1924) Correlation in seasonal variations of weather, IV, A further study of world weather. Memoirs of the Indian Meteorol Dept 24:275-332

Wang B (2006) The Asian monsoon. B Wang (ed) Springer-Verlag, Berlin, Germany

Wang B, Fan Z (1999) Choice of South Asian summer monsoon indices. Bull Amer Meteorol Soc 80:629-638

Wang B, LinHo (2002) Rainy season of the Asian-Pacific Summer Monsoon. J Clim 15:386-398

Wang B, Xie X (1997) A model for the boreal summer intraseasonal oscillation. J Atmos Sci 54:72-86

Wang B, Kang I-S, Lee J-Y (2004) Ensemble simulations of Asian-Australian monsoon variability by 11 AGCMs. J Clim, 17:803-818

Wang B, Wu Z, Li J, Liu J, Chang C-P, Ding Y, Wu G (2008) How to measure the strength of the East Asian summer monsoon. J Clim 21:4449-4463

Watanabe M, Suzuki T, O'ishi R, Komuro Y, Watanabe S, Emori S, Takemura T, Chikira M, Ogura T, Sekiguchi M, Takata K, Yamazaki D, Yokohata T, Nozawa T, Hasumi H, Tatebe H, Kimoto M (2010) Improved climate simulation by MIROC5: mean states, variability, and climate sensitivity. J Clim 23:6312-6335. doi:10.1175/2010JCLI3679.1

WCRP, 1992: Simulation of interannual and intraseasonal monsoon variability. Rept. of Workshop, Boulder, Colorado, USA, 21-24 Oct. 1991. WCRP-68, WMP/TD-470, WCRP, Geneva, Switzerland

WCRP, 1993: Simulation and prediction of monsoons: Recent results (TOGA/WGNE Monsoon). Numerical Experimentation Group, New Delhi, India, 12-14 Jan. 1993. WCRP-80, WMP/TD-546, WCRP, Geneva, Switzerland

Webster PJ, Jian J (2011) Environmental prediction, risk assessment and extreme events: adaptation strategies for the developing world. Phil Tran R Soc A 369:4768-4797. doi:10.1098/rsta.2011.0160

Webster PJ, Magana VO, Palmer TN, Shukla J, Thomas RA, Yanai M, Yasunari T (1998) Monsoons: Processes, predictability, and the prospects for prediction. J Geophys Res 103:14,451-14,510

Wilks DS Statistical methods in the atmospheric sciences. Academic Press, San Diego, California, USA

Wittenberg AT (2009) Are historical records sufficient to constrain ENSO simulations? Geophys Res Lett 36:L12702. doi:10.1029/2009GL038710

Wu B, Zhou T (2012) Relationships between East Asian-western North Pacific monsoon and ENSO simulated by FGOALS-s2. Adv Atmos Sci (in press)

Wu G, Gan Y, Liu Y, Yan J, Mao J (2012) Air–sea interaction and formation of the Asian summer monsoon onset vortex over the Bay of Bengal. Clim Dyn 38:261-279. doi:10.1007/s00382-010-0978-9

Xie PP, Arkin PA (1997) Global precipitation: A 17-year monthly analysis based on gauge observations, satellite estimates, and numerical model outputs. Bull Amer Meteorol Soc 78:2539–2558

Zhou T, Li Z (2002) Simulation of the east Asian summer monsoon by using a variable resolution atmospheric GCM. Clim Dyn 19:167-180

Zhou T, Yu R-C (2005) Atmospheric water vapor transport associated with typical anomalous summer rainfall patterns in China. J Geophys Res 110:D08104. doi:10.1029/2004JD005413

Zhou T, Zou L (2010) Understanding the Predictability of East Asian Summer Monsoon from the Reproduction of Land-Sea Thermal Contrast Change in AMIP-type Simulation, J Clim 23:6009-6026. doi:10.1175/2010JCLI3546.1

Zhou T, Hsu H-H, Matsumoto J (2011) Summer monsoons in East Asian Indochina, and the western North Pacific. In: Chang C-P, Ding Y, Lau N-C, Johnson RH, Wang B, Yasunari T (eds) The Global Monsoon System, Research and Forecast, 2nd edn. World Scientific Publishing Co, Singapore, pp 43-72

Zhou T, Wu B, Wang B, (2009a) How Well Do Atmospheric General Circulation Models Capture the Leading Modes of the Interannual Variability of the Asian-Australian Monsoon? J Clim 22:1159-1173

Zhou T, Gong D, Li J, Li B (2009b) Detecting and understanding the multi-decadal variability of the East Asian Summer Monsoon – Recent progress and state of affairs. Meteorologische Zeitschrift, 18:455-467

Zhou T, Wu B, Scaife AA, Bronnimann S, Cherchi A, Fereday D, Fischer AM, Folland CK, Jin KE, Kinter J, Knight JR, Kucharski F, Kusunoki S, Lau N-C, Li L, Nath MJ, Nakaegawa T, Navarra A, Pegion P, Rozanov E, Schubert S, Sporyshev P, Voldoire A, Wen X, Yoon JH, Zeng N (2009c) The CLIVAR C20C Project: Which components of the Asian-Australian Monsoon circulation variations are forced and reproducible? Clim Dynam, 33:1051–1068. doi:10.1007/s00382-008-0501-8

Table Captions

Table 1: Modeling group, model designation, and horizontal and vertical resolution of the atmospheric and oceanic models, respectively. Capitalized designations are CMIP5 models, and lower-case designations are CMIP3 models

Table 2: Skill scores for the June-September climatology and the climatological annual cycle. The results are given for observations, the MMM's, and for the CMIP5 and CMIP3 models. The observed skill for precipitation is between GPCP and CMAP, and the skill for the 850hPa wind (850hPa) is between ERA40 and JRA25. The model pattern correlations for the precipitation climatology (Pr) are calculated with respect to GPCP precipitation. For the 850hPa wind climatology (850hPa), the model pattern correlations are calculated with respect to ERA40 850hPa wind. For the climatologies the skill is calculated over the region 40^{o}E-160^{o}E, 20^{o}S-50^{o}N. For the time-latitude (T-Lat) climatological annual cycle of monthly rainfall averaged between 70^{o}E-90^{o}E, the model pattern correlations are calculated with respect to GPCP precipitation over the region 10^{o}S-30^{o}N, for May-October (see Section 4.1). For the climatological annual cycle of pentad rainfall, the model pattern correlations are calculated with respect to GPCP precipitation for the pentads of onset, peak, withdrawal, and duration of the monsoon over the region 50^{o}E-180^{o}E, 0^{o}-50^{o}N (see Section 4.2). The categorical skill scores, hit rate and threat score, indicate how well a model represents the spatial domain of the monsoon, where a value = 1 indicates perfect agreement between model and observations. Missing table entries occur for models that did not have available data for analysis. The top five models with the largest skill scores for each diagnostic are highlighted

Table 3: Skill scores for the Indian Monsoon and East Asian Monsoon interannual variability and the boreal summer intraseasonal variability (BSISV). The results are given for observations, the MMM's, and for the CMIP5 and CMIP3 models. The interannual variations of the ENSO-Monsoon relationship are characterized by (1) the lag 0 correlation between JJAS anomalies of all-India rainfall and Niño3.4 SST (AIR/N3.4). The AIR is for land-only gridpoints over the region 65^{o}E-95^{o}E, 7^{o}N-30^{o}N. The observations are for the anomalies of Rajeevan rainfall vs. HadISST SST for 1961-1999, and (2) the pattern correlations of JJAS precipitation anomalies (Pr) obtained from regression with JJAS anomalies of Niño3.4 SST. The model pattern correlations are calculated with respect to GPCP anomalies that were obtained by regression with the Niño3.4 SST anomalies from the NCEP/NCAR reanalysis (1979-2007). The pattern correlations are calculated over the region 60^{o}E-100^{o}E, 0^{o}-30^{o}N. For observations the skill is between GPCP and CMAP. For the East Asian Monsoon, the negative of the June-August Wang and Fan (1999) zonal wind shear index (WFN, see Section 5.2) is regressed against June-August anomalies of precipitation and 850hPa wind. The model pattern correlations are calculated with respect to GPCP rainfall anomalies and JRA 850hPa wind anomalies that were obtained by regression with the JRA25 WFN. The pattern correlations are calculated over the region 100^{o}E-140^{o}E, 0^{o}-50^{o}N. For observations the skill is between GPCP/JRA25 and CMAP/NCEP-NCAR Reanalysis. For BSISV, the skill is (1) the pattern correlation of June-September 20-100 day

bandpass filtered OLR variance between the model (1961-1999) and AVHRR OLR (1979-2006). For observations the skill is for AVHRR OLR for 1979-2006 vs. AVHRR OLR for 1979-1995, and (2) the spatio-temporal correlation of the model BSISV life cycle vs. that from the observed cyclostationary EOF (CsEOF) analysis of Annamalai and Sperber (2005). The life cycle of the BSISV is obtained by first projecting 20-100 day filtered OLR from observations (1979-2006) and the models (1961-1999) on to the Day 0 pattern of the observed CsEOF. The resulting PC is used for lag regression against the 20-100 day filtered OLR with the spatio-temporal correlation between model and observation being calculated for Day -15, Day -10, Day -5, Day 0, Day 5, Day 10, Day 15, and Day 20 . The skill scores for the intraseasonal variability are calculated over the region 40^oE-180^oE, 30^oS-30^oN. Missing table entries occur for models that did not have available data for analysis. The top five models with the largest skill scores for each diagnostic are highlighted

Table 1

Modelling Group	Model Designation	AGCM horizontal/vertical resolution	OGCM horizontal/vertical resolution
Beijing Climate Center, China Meteorological Administration	BCC-CSM1.1	T42 L26	1^{o} lon x 1.33^{o} lat L40
Bjerknes Center for Climate Research	bccr-bcm2.0	T63 L31	1.5^{o} lon x 0.5^{o} -1.5^{o}cos(lat) L35
Canadian Centre for Climate Modelling and Analysis	CanESM2 cgcm3.1 (t47) cgcm3.1 (t63)	T63 L35 T47 L31 T63 L31	256 x 192 L40 192 x 96 L29 256 x 192 L31
National Center for Atmospheric Research	CCSM4 ccsm3 pcm1	1.25^{o} lon x 0.9^{o} lat L26 T85 L26 T42 L 18	1.1^{o} lon x 0.27^{o}-0.54^{o} lat L60 384 x 288 L32 384 x 288 L32
Centre National de Recherches Meteorologiques/Centre Europeen de Recherche et Formation Avancees en Calcul Scientifique	CNRM-CM5 cnrm-cm3	TL127 L31 T42 L45	1^{o} lon x 1^{o} lat L42 180 x 170 L33
Commonwealth Scientific and Industrial Research Organization in collaboration with Queensland Climate Change Centre of Excellence	CSIRO-Mk3.6.0 csiro-mk3.0 csiro-mk3.5	T63 L18 T63 L18 T63 L18	1.875^{o} lon x ~0.9375^{o} lat L31 1.875^{o} lon x 0.925^{o} lat L31 1.875^{o} lon x 0.925^{o} lat L31
Meteorological Institute of the University of Bonn, Meteorological Research Institute of KMA, and Model and Data group	echo-g	T30 L19	T42 L20
LASG, Institute of Atmospheric Physics, Chinese Academy of Sciences and CESS,Tsinghua University	FGOALS-g2	128 x 60 L26	360 x 196 L30

LASG, Institute of Atmospheric Physics, Chinese Academy of Sciences	FGOALS-s2 fgoals-g1.0	R42 L26 T42 L26	0.5^o-1^o lon x 0.5^o-1^o lat L 1^o lon x 1^o lat L16
NOAA Geophysical Fluid Dynamics Laboratory	GFDL-CM3 GFDL-ESM2G GFDL-ESM2M gfdl-cm2.0 gfdl-cm2.1	C48 L48 M45 L24 M45 L24 N45 L24 N45 L24	360 x 200 L50 360 x 210 L63 360 x 200 L50 1^o lon x 0.33^o -1^o lat L50 1^o lon x 0.33^o -1^o lat L50
NASA Goddard Institute for Space Studies	GISS-E2-H GISS-E2-R giss-aom	2.5^o lon x 2^o lat L40 2.5^o lon x 2^o lat L40 90 x 60 L12	1.25^o lon x 1^o lat L32 1^o lon x ~1^o lat L32 90 x 60 L16
Met Office Hadley Centre	HadCM3 HadGEM2-CC HadGEM2-ES ukmo-hadcm3 ukmo-hadgem1	N48 L19 N96 L60 N96 L38 2.5^o lon x 3.75^o lat L19 N96 L38	1.25^o lon x 1.25^o lat L20 1^o lon x 0.3^o-1.0^o lat L40 1^o lon x 0.3^o-1.0^o lat L40 1.25^o lon x 1.25^o lat L20 1^o lonn x 0.3^o-1.0^o lat L40
Instituto Nazionale di Geofisica e Volcanologia	ingv-sxg	T106 L19	1^o lon x 1^o lat L31
Institute for Numerical Mathematics	INM-CM4 inm-cm3.0	2^o lon x 1.5^o lat L21 5^o lon x 4^o lat L21	1^o lon x 0.5^o lat L40 2.5^o lon x 2^o lat L33
Institut Pierre-Simon Laplace	IPSL-CM5A-LR IPSL-CM5A-MR ipsl-cm4	96 x 95 L39 144 x 143 L39 96 x 72 L19	2^o lon x 2^o lat L31 2^o lon x 2^o lat L31 2^o lon x 2^o lat L31
Japan Agency for Marine-Earth Science and Technology, Atmosphere and Ocean Research Institute (The University of Tokyo), and National Institute for Environmental Studies	MIROC-ESM MIROC-ESM-CHEM	T42 L80 T42 L80	256 x 192 L44 256 x 192 L44
Atmosphere and Ocean Research Institute (The University of Tokyo), National Institute for Environmental Studies, and Japan Agency for Marine-Earth Science and Technology	MIROC4h MIROC5 miroc3.2(hires) miroc3.2(medres)	T213 L56 T85 L40 T106 L56 T42 L20	1280 x 912 L48 256 x 224 L50 T106 L48 256 x 192 L44
Max Planck Institute for Meteorology	MPI-ESM-LR echam5/mpi-om	T63 L47 T63 L32	GR15 L40 1^o lon x 1^o lat L42

Meteorological Research Institute	MRI-CGCM3 mri-cgcm2.3.2	TL159 L48 T42 L30	1^{o} lon x 0.5^{o} lat L51 256 x 192 L44
Norwegian Climate Centre	NorESM1-M	144 x 96 L26	384 x 320 L53

Table 2

Model	Climatology		Climatological Annual Cycle Rainfall						
	Pr	850hPa	T-Lat	Onset	Peak	Withd.	Duration	Hit Rate	Threat
Observations	0.927	0.986	0.887	0.748	0.834	0.830	0.671	0.893	0.744
CMIP5 MMM	0.898	0.976	0.674	0.664	0.786	0.792	0.605	0.844	0.625
CMIP3 MMM	0.865	0.967	0.657	0.510	0.733	0.712	0.380	0.821	0.573
BCC-CSM-1	0.808	0.928	0.338						
bccr-bcm2.0	0.733	0.933	0.639						
CanESM2	0.815	0.951	0.552	0.298	0.451	0.543	0.164	0.782	0.517
cgcm3.1 (t47)	0.782	0.935	0.465	0.063	0.476	0.454	0.109	0.766	0.522
cgcm3.1 (t63)	0.796	0.944	0.461	0.155	0.432	0.384	0.154	0.758	0.508
CCSM4	**0.849**	0.952	0.678	0.581	**0.717**	**0.798**	**0.570**	**0.836**	**0.619**
ccsm3	0.748	0.913	0.390	0.394	0.481	0.459	0.346	0.757	0.487
pcm1	0.634	0.793	0.364						
CNRM-CM5	**0.852**	**0.974**	0.567	**0.674**	0.638	0.750	**0.656**	0.796	0.513
cnrm-cm3	0.717	0.908	**0.763**	0.489	0.596	0.633	0.329	0.749	0.437
CSIRO-Mk3.6.0	0.713	0.896	0.232	0.006	0.451	0.729	0.331	0.762	0.497
csiro-mk3.0	0.803	0.889	0.385	0.196	0.461	0.601	0.147	0.790	0.495
csiro-mk3.5	0.796	0.923	0.171	0.287	0.474	0.665	0.350	0.788	0.540
FGOALS-g2	0.766	0.923	0.455						
FGOALS-s2	0.807	0.916	0.613	**0.601**	0.596	0.649	0.531	0.812	0.537
fgoals-g1.0	0.690	0.803	0.587	-0.050	**0.672**	**0.785**	0.097	0.770	0.460
GFDL-CM3	**0.844**	0.941	**0.742**	0.458	0.407	0.546	0.406	0.796	0.532
GFDL-ESM2G	0.821	**0.955**	**0.727**	0.370	0.560	0.660	0.328	**0.841**	**0.615**
GFDL-ESM2M	0.828	**0.958**	0.676	0.490	**0.714**	0.730	0.383	0.824	0.586
gfdl-cm2.0	0.826	**0.954**	0.673	**0.715**	0.540	0.624	0.495	0.812	0.559
gfdl-cm2.1	**0.843**	**0.957**	**0.681**	0.453	0.662	0.731	0.485	0.825	0.587
GISS-E2-H	0.631	0.902	0.318						
GISS-E2-R	0.730	0.912	0.235						
giss-aom	0.780	0.894	0.282	0.359	0.614	0.540	0.203	0.774	0.457
HadCM3	0.773	0.931	0.550	0.555	0.447	0.519	0.452	**0.873**	**0.675**
HadGEM2-CC	0.795	0.927	0.376	0.526	0.659	0.634	0.317	0.777	0.543
HadGEM2-ES	0.800	0.933	0.356	0.562	0.620	0.648	0.367	0.769	0.538
ukmo_hadcm3	0.778	0.932	0.529						
ukmo_hadgem1	0.798	0.938	0.386						
ingv-sxg	0.814	0.950	0.629	0.277	0.575	0.724	0.417	0.797	0.516
INM-CM4	0.742	0.864	0.561	0.153	0.616	0.649	0.224	0.810	0.560
inm-cm3.0	0.619	0.837	0.497	-0.125	0.331	0.592	-0.064	0.795	0.517
IPSL-CM5A-LR	0.797	0.926	0.442	0.399	0.540	0.712	0.482	0.798	0.515
IPSL-CM5A-MR	0.809	0.935	0.501	0.421	0.575	**0.769**	**0.591**	0.787	0.501
ipsl-cm4	0.743	0.907	0.214	0.215	0.495	0.634	0.254	0.786	0.468
MIROC-ESM	0.617	0.824	0.518	0.391	0.610	0.666	0.394	0.756	0.434
MIROC-ESM-CHEM	0.642	0.831	0.538	0.518	0.669	0.653	0.423	0.752	0.433
MIROC4h	0.802	0.940	0.573	**0.674**	0.626	0.766	**0.620**	**0.843**	**0.611**
MIROC5	0.842	0.940	**0.778**	0.362	**0.778**	**0.851**	**0.652**	0.808	0.531
miroc3.2(hires)	0.761	0.914	0.523	0.483	0.383	0.709	0.568	0.792	0.486
miroc3.2(medres)	0.765	0.919	0.513	**0.633**	0.402	0.571	0.503	0.744	0.384
MPI-ESM-LR	0.792	0.949	0.664	0.316	0.579	0.652	0.472	0.781	0.535
echam5/mpi-om	0.800	0.942	0.664	0.265	0.412	0.537	0.337	0.800	0.547
echo_g	0.803	0.911	0.522	0.008	0.041	0.368	0.189	0.787	0.507
MRI-CGCM3	0.752	0.886	0.195	0.024	0.619	0.535	-0.014	0.751	0.465
mri-cgcm2.3.2	0.726	0.885	0.538	0.471	0.345	0.550	0.346	0.746	0.473
NorESM1-M	**0.848**	0.913	0.634	0.558	**0.723**	**0.791**	0.565	**0.838**	**0.624**

Table 3

Model	Indian Monsoon		East Asian Monsoon		BSISV	
	AIR/N3.4	Pr	Pr	850hPa	Variance	Life Cycle
Observations	-0.533	0.798	0.959	0.989	0.995	0.893
CMIP5 MMM		0.616	0.888	0.972	0.903	0.766
CMIP3 MMM		0.600	0.799	0.969	0.895	0.754
BCC-CSM-1	-0.250	-0.140	0.695	0.930		
bccr-bcm2.0	-0.430	0.249	0.670	**0.951**		
CanESM2	-0.273	0.014	0.672	0.861	0.846	0.651
cgcm3.1 (t47)	-0.335	0.404	0.625	0.899	0.727	0.605
cgcm3.1 (t63)	-0.182	0.173	0.703	0.938	0.717	0.604
CCSM4	-0.556	0.337	**0.789**	0.947		
ccsm3	-0.561	0.264	0.722	0.800	0.695	0.588
pcm1	-0.356	0.293	0.232	0.870		
CNRM-CM5	-0.307	0.245	0.642	0.894		
cnrm-cm3	-0.484	0.419	0.313	0.727	0.570	0.600
CSIRO-Mk3.6.0	-0.487	0.162	0.346	0.858	0.809	0.645
csiro-mk3.0	-0.403	-0.112	0.629	0.939	0.830	0.581
csiro-mk3.5	**-0.719**	0.137	0.569	0.924		
FGOALS-g2	-0.052	0.238	0.739	0.936		
FGOALS-s2	0.114	0.096	0.787	0.921	0.734	0.608
fgoals-g1.0	**-0.747**	0.276	0.415	0.426	0.271	0.438
GFDL-CM3	-0.442	0.192	0.315	0.867		
GFDL-ESM2G	-0.289	0.251	0.458	**0.972**	0.753	0.643
GFDL-ESM2M	-0.187	0.251	0.606	**0.955**		
gfdl-cm2.0	-0.667	0.336	0.668	**0.976**	0.818	0.677
gfdl-cm2.1	-0.494	0.412	0.390	0.919	**0.850**	**0.712**
GISS-E2-H	-0.094	0.254	0.586	0.918		
GISS-E2-R	-0.366	0.379	0.656	0.906		
giss-aom	0.094	0.189	0.117	0.754	-0.070	0.395
HadCM3	-0.299	0.180	0.773	0.897		
HadGEM2-CC	-0.335	-0.068	**0.787**	0.935	**0.857**	0.641
HadGEM2-ES	-0.344	0.216	**0.839**	0.949	**0.862**	0.651
ukmo-hadcm3	-0.374	0.323	0.758	0.947		
ukmo-hadgem1	-0.446	0.154	0.744	0.912		
ingv-sxg	-0.455	0.313	0.513	0.925		
INM-CM4	-0.033	0.110	-0.047	0.816	0.639	0.562
inm-cm3.0	-0.258	-0.073	0.520	0.850		
IPSL-CM5A-LR	**-0.700**	**0.611**	0.450	0.708	0.791	0.654
IPSL-CM5A-MR	**-0.763**	**0.636**	0.532	0.749	0.827	0.635
ipsl-cm4	-0.554	0.347	0.675	0.787	0.785	0.648
MIROC-ESM	0.088	0.061	0.596	0.694	0.548	0.516
MIROC-ESM-CHEM	-0.104	0.045	0.687	0.882	0.554	0.528
MIROC4h	-0.327	**0.529**	0.723	0.921	0.736	0.625
MIROC5	-0.321	0.010	0.567	0.946	0.805	**0.691**
miroc3.2(hires)	0.080	-0.009	0.643	0.915	0.666	0.543
miroc3.2(medres)	-0.329	0.234	0.719	0.928	0.800	0.575
MPI-ESM-LR	-0.291	0.401	0.283	0.899	**0.874**	**0.681**
echam5/mpi-om	-0.573	**0.560**	0.230	0.817	**0.873**	**0.721**
echo_g	-0.554	0.113	0.664	0.914	0.810	**0.702**
MRI-CGCM3	-0.274	0.338	**0.819**	0.937	0.782	0.628
mri-cgcm2.3.2	-0.424	0.107	0.570	0.931	0.575	0.654
NorESM1-M	**-0.690**	**0.522**	**0.811**	**0.959**	0.833	0.627

Figure Captions

Fig. 1 a-e JJAS precipitation rate climatology from **a** GPCP, **b** CNRM-CM5, **c** MIROC-ESM, **d** CMIP5 MMM, and **e** CMIP3 MMM. Also given in **a** is the pattern correlation of GPCP with CMAP, and in **b-e** are the model pattern correlations with GPCP over the region 40^{o}E-160^{o}E, 20^{o}S-50^{o}N. **f** (CMAP) *minus* (GPCP), **g-j** as **b-e** but for (model) *minus* (GPCP). The units are (mm day^{-1}). GPCP and CMAP data is from 1979-2007 and the model data is from 1961-1999

Fig. 2 a-e JJAS 850hPa wind climatology from **a** ERA40, **b** CNRM-CM5, **c** pcm1, **d** CMIP5 MMM, and **e** CMIP3 MMM. Also given in **a** is the pattern correlation of ERA40 with JRA25, and in **b-e** are the model pattern correlations with ERA40 over the region 40^{o}E-160^{o}E, 20^{o}S-50^{o}N. (f) (JRA25) *minus* (ERA40), **g-j** as **b-e** but for (model) *minus* (ERA40). The units are (ms^{-1}). ERA40 and the model data are from 1961-1999, and JRA25 data is from 1979-2007

Fig. 3 Scatterplot of the pattern correlation with observations of simulated JJAS 850hPa wind climatology vs. the pattern correlation with observations of simulated JJAS precipitation climatology. The skill is relative to ERA40 and GPCP over the region 40^{o}E-160^{o}E, 20^{o}S-50^{o}N

Fig. 4 a-f Annual cycle climatology for rainfall rate averaged between 70^{o}E-90^{o}E from **a** GPCP, **b** CMAP, **c** MIROC5, **d** csiro-mk3.5, **e** CMIP5 MMM, and **f** CMIP3 MMM. Also given in **b-f** is the pattern correlation with GPCP over the region 10^{o}S-30^{o}N, for May-September (the dashed region in **a**). The units are (mm day^{-1}). **g** Models stratified by their pattern correlation with GPCP. GPCP and CMAP data are from 1979-2007 and the model data is from 1961-1999

Fig. 5 The relative rainfall rate over the Bay of Bengal (85^{o}E-90^{o}E, 7.5^{o}N-20^{o}N) from GPCP data. The 5 mm day^{-1} threshold is used to define the pentads of onset and withdrawal of the monsoon. To calculate the relative rainfall rate, the pentad time series is smoothed with a five pentad running mean. The January mean rainfall is then removed from each pentad, resulting in the relative rainfall rate. See Section 4.2 for more details

Fig. 6 Monsoon onset pentad **a** GPCP, **b** gfdl cm2.0, **c** inm-cm 3.0, **d** CMIP5 MMM, and **e** CMIP3 MMM. Monsoon peak pentad **f** GPCP, **g** MIROC5, **h** echo-g, **i** CMIP5 MMM, and **j** CMIP3 MMM. Also given in **a** and **f** is the pattern correlation of GPCP with CMAP, and in **b-e** and **g-j** are the model pattern correlations with GPCP over the region 50^{o}E-180^{o}E, 0^{o}-50^{o}N. The units are pentad (Pentad 1 = January 1-5). Note the difference in scale for the onset vs. peak phases. GPCP and CMAP data are from 1979-2007 and the model data is from 1961-1999

Fig. 7 Monsoon withdrawal pentad **a** GPCP, **b** MIROC5, **c** echo-g, **d** CMIP5 MMM, and **e** CMIP3 MMM. Monsoon duration **f** GPCP, **g** CNRM-CM5, **h** inm-cm3.0, **i** CMIP5 MMM, and **j** CMIP3 MMM. Also given in **a** and **f** is the pattern correlation of GPCP with CMAP, and in **b-e** and **g-j** are the model pattern correlations with GPCP over the region 50^{o}E-180^{o}E, 0^{o}-50^{o}N. For withdrawal the units are pentad (Pentad 1 = January 1-5). For duration the units are the number of pentads based on (withdrawal) *minus* (onset) pentad. GPCP and CMAP data are from 1979-2007 and the model data is from 1961-1999

Fig. 8 Scatterplot of the pattern correlation with observations of the simulated pentad of monsoon onset vs. **a** the pattern correlation with observations of the simulated pentad of monsoon peak, **b** the pattern correlation with observations of the simulated pentad of monsoon withdrawal, and **c** the pattern correlation with observations of the simulated number of pentads of monsoon duration. **d** Scatterplot of the Monsoon Domain Hit Rate vs. the Monsoon Domain Threat Score. In **a-d** the skill is with respect to GPCP for the region 50^{o}E-180^{o}E, 0^{o}-50^{o}N

Fig. 9 a The ENSO-monsoon relationship skill is given by the lag 0 correlation between interannual JJAS anomalies of AIR and Niño3.4 SST. The AIR is for land-only gridpoints over 65^{o}E-95^{o}E, 7^{o}N-30^{o}N. The results are given for the Rajeevan rainfall data vs. HadISST SST (1961-1999; black), GPCP rainfall vs. SST used in the NCEP-NCAR Reanalysis (1979-2007; violet), CMIP5 models (1961-1999; red), and the CMIP3 models (1961-1999; green). The thick black dashed line is the 5% significance level assuming each year is independent for 37 degrees of freedom. **b** The AIR-Niño3.4 SST correlations in **a** are plotted vs. the pattern correlations of the interannual JJAS precipitation anomalies (mm day^{-1}) from linear regression with JJAS Niño3.4 SST anomalies (see Fig. 10). The pattern correlations are calculated with respect to GPCP over the region 60^{o}E-100^{o}E, 0^{o}-30^{o}N

Fig. 10 Interannual JJAS precipitation anomalies (mm day^{-1}) from linear regression with JJAS Niño3.4 SST anomalies **a** Rajeevan rainfall data vs. HadISST SST (1961-1999), **b** GPCP rainfall vs. SST used in the NCEP-NCAR Reanalysis (1979-2007), **c** IPSL-CM5A-MR, **d** FGOALS-s2, **e** CMIP5 MMM, and **f** CMIP3 MMM. The regressions are scaled by one standard deviation of the Niño3.4 SST anomalies and are thus consistent with anomalies during El Niño. **c** and **d** are the models that span the range of the AIR-Niño3.4 SST correlations from the CMIP5 and CMIP3 models (see Figure 9a). In panels **a-d** the first (or only) value is the correlation of AIR-Niño3.4 SST. The last value in **b** is the pattern correlation of GPCP with CMAP for the interannual JJAS precipitation anomalies, and in **c-f** the last (or only) value is the model pattern correlation with GPCP for the interannual JJAS precipitation anomalies. The skill metrics are calculated over the region 60^{o}E-100^{o}E, 0^{o}-30^{o}N. The Rajeevan rainfall, the HadISST SST, and the model data is for 1961-1999. The GPCP, CMAP and NCEP-NCAR Reanalysis SST data are for 1979-2007

Fig. 11 Interannual East Asian summer monsoon JJA 850hPa wind anomalies and precipitation anomalies from linear regression with the revised JJA Wang-Fan 850hPa zonal wind index for **a** JRA25/GPCP, **b** CMIP5 MMM, **c** CMIP3 MMM, **d** gfdl cm2.0 model, **e** fgoals-g1.0, **f** HadGEM2-ES, and **g** INM-CM4. **d** and **e** are the models with the largest and smallest 850hPa wind pattern correlations compared to JRA25 850hPa wind anomalies, and **f** and **g** are the models with the largest and smallest precipitation pattern correlations compared to GPCP. Also given in **a** is the pattern correlation of JRA25 with NCEP/NCAR Reanalysis and GPCP with CMAP, respectively, and in **b-g** are the model pattern correlations with JRA25 and GPCP over the region 100^{o}E-140^{o}E, 0^{o}-50^{o}N. The units for the 850hPa wind anomalies are ms^{-1} and for precipitation anomalies the units are mm day^{-1}. The JRA25 reanalysis, the NCEP-NCAR reanalyses, the GPCP, and CMAP data are for 1979-2007. The model data is for 1961-1999

Fig. 12 a Scatterplot of the pattern correlation with observations of simulated JJA 850hPa wind anomalies vs. the pattern correlation with observations of simulated JJA precipitation anomalies over East Asia. The skill is relative to JRA25 and GPCP over the region 100^{o}E-140^{o}E, 0^{o}-50^{o}N. **b** Scatterplot of the pattern correlation with observations of simulated JJA 850hPa wind anomalies vs. the pattern correlation with observations of the simulated JJA 850hPa wind climatology. The skill is with respect to JRA25 on the x-axis, and with respect to ERA40 on the y-axis. **c** Scatterplot of the pattern correlation with GPCP of simulated JJA precipitation anomalies vs. the pattern correlation with observations of the simulated JJA precipitation climatology. **d** Scatterplot of the pattern correlation with GPCP of simulated JJA precipitation anomalies over the East Asia (as in Figs. 12a and 12c) vs. the pattern correlation with GPCP of simulated JJAS precipitation anomalies over the Indian Summer Monsoon (as in Fig. 9b)

Fig. 13 20-100 day bandpass filtered OLR variance for JJAS from **a** AVHRR (1979-2006), **b** MPI-ESM-LR, **c** MIROC-ESM, **d** MIROC5, **e** CMIP5 MMM, and **f** CMIP3 MMM. Also given in **a** is the pattern correlation with AVHRR OLR for 1979-1995, and in **b-f** are the model pattern correlations with AVHRR OLR (1979-2006) over the region 40^{o}E-180^{o}E, 30^{o}S-30^{o}N. The model data is for 1961-1999

Fig. 14 Lag regression of 20-100 day bandpass filtered AVHRR OLR with PC-4 for JJAS 1979-2006 for **a** Day -15 to **h** Day 20. The lag regressions have been scaled by one standard deviation of PC-4 to give units of W m^{-2}. The pattern correlations are calculated with respect to Day -15, Day -10, Day -5, Day 0, Day 5, Day 10, Day 15, and Day 20 of the CsEOF of Annamalai and Sperber (2005) over the region 40^{o}E-180^{o}E, 30^{o}S-30^{o}N. Data are plotted where the regressions are statistically significant at the 5% level, assuming each pentad is independent

Fig. 15 Scatterplot of the pattern correlation with observations of the simulated JJAS 20-100 day bandpass filtered OLR variance vs. the space-time pattern correlation with observations of the simulated JJAS BSISV life-cycle. For the variance, the observed and simulated skill is calculated with respect to AVHRR OLR for JJAS 1979-2006. The observed variance skill is calculated using the JJAS 20-100 day bandpass filtered OLR variance for 1979-1995. For BSISV, the skill is for the models best matching patterns with respect to Day -15, Day -10, Day -5, Day 0, Day 5, Day 10, Day 15, and Day 20 of the CsEOF given in Annamalai and Sperber (2005). The observed (1979-2006) and simulated BSISV life-cycle is recovered from linear regression with PC-4 obtained by projecting 20-100 day bandpass filtered OLR onto the Day 0 CsEOF pattern from Annamalai and Sperber (2005). The skill scores are calculated over the region 40^{o}E-180^{o}E, 30^{o}S-30^{o}N

Fig. 16 As Fig. 14, but for MIROC5 20-100 day bandpass filtered JJAS OLR (1961-1999)

Fig. 17 As Fig. 14, but for the CMIP5 MMM. For each time lag, and at each gridpoint, the average anomaly is plotted if more than half of the models have a statistically significant convective anomaly, irrespective of sign

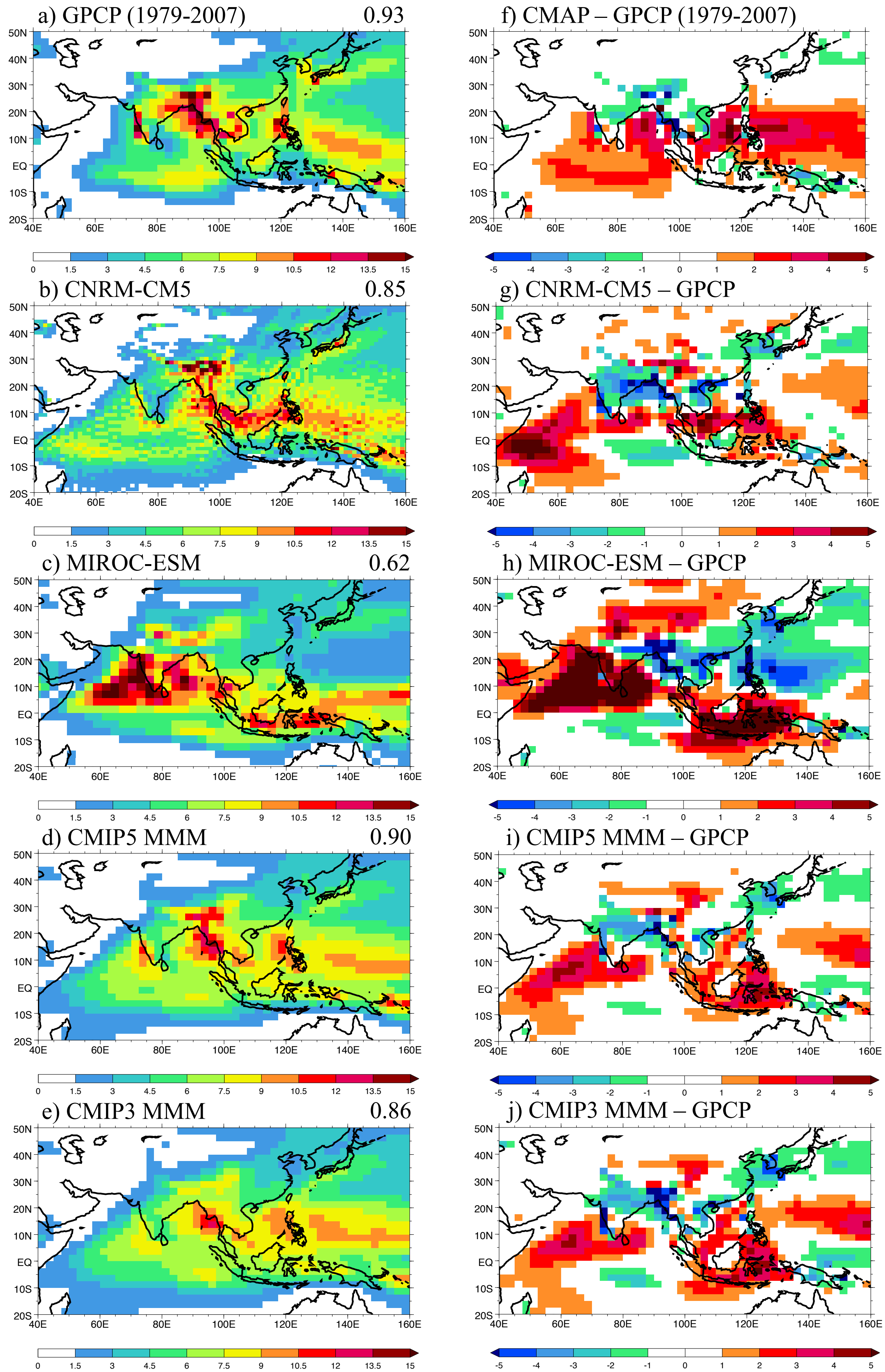

Fig. 1 a-e JJAS precipitation rate climatology from **a** GPCP, **b** CNRM-CM5, **c** MIROC-ESM, **d** CMIP5 MMM, and **e** CMIP3 MMM. Also given in **a** is the pattern correlation of GPCP with CMAP, and in **b-e** are the model pattern correlations with GPCP over the region 40°E-160°E, 20°S-50°N. **f** (CMAP) *minus* (GPCP), **g-j** as **b-e** but for (model) *minus* (GPCP). The units are (mm day^{-1}). GPCP and CMAP data is from 1979-2007 and the model data is from 1961-1999

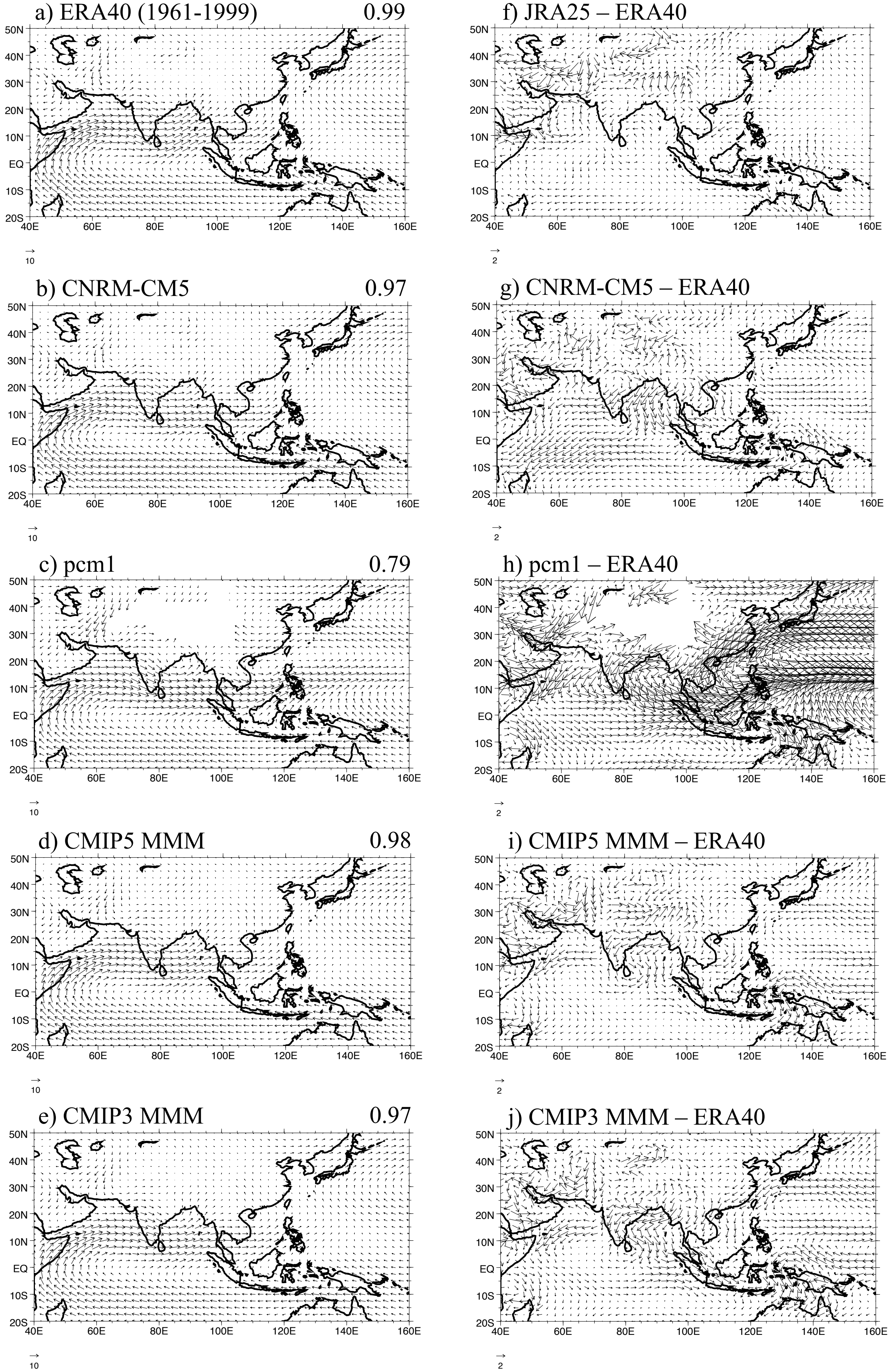

Fig. 2 a-e JJAS 850hPa wind climatology from **a** ERA40, **b** CNRM-CM5, **c** pcm1, **d** CMIP5 MMM, and **e** CMIP3 MMM. Also given in **a** is the pattern correlation of ERA40 with JRA25, and in **b-e** are the model pattern correlations with ERA40 over the region 40°E-160°E, 20°S-50°N. (f) (JRA25) *minus* (ERA40), **g-j** as **b-e** but for (model) *minus* (ERA40). The units are (ms^{-1}). ERA40 and the model data are from 1961-1999, and JRA25 data is from 1979-2007

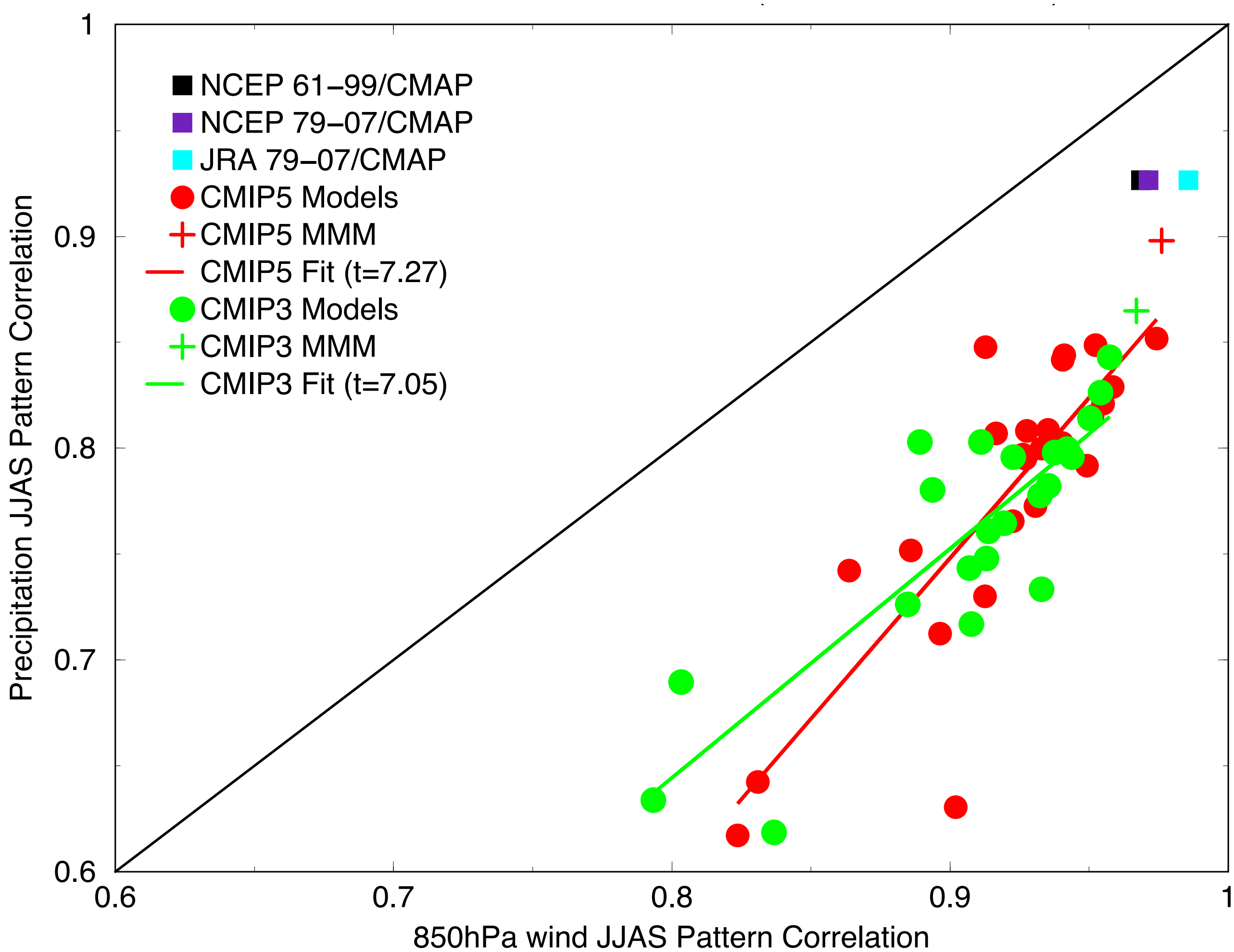

Fig. 3 Scatterplot of the pattern correlation with observations of simulated JJAS 850hPa wind climatology vs. the pattern correlation with observations of simulated JJAS precipitation climatology. The skill is relative to ERA40 and GPCP over the region 40^{o}E-160^{o}E, 20^{o}S-50^{o}N

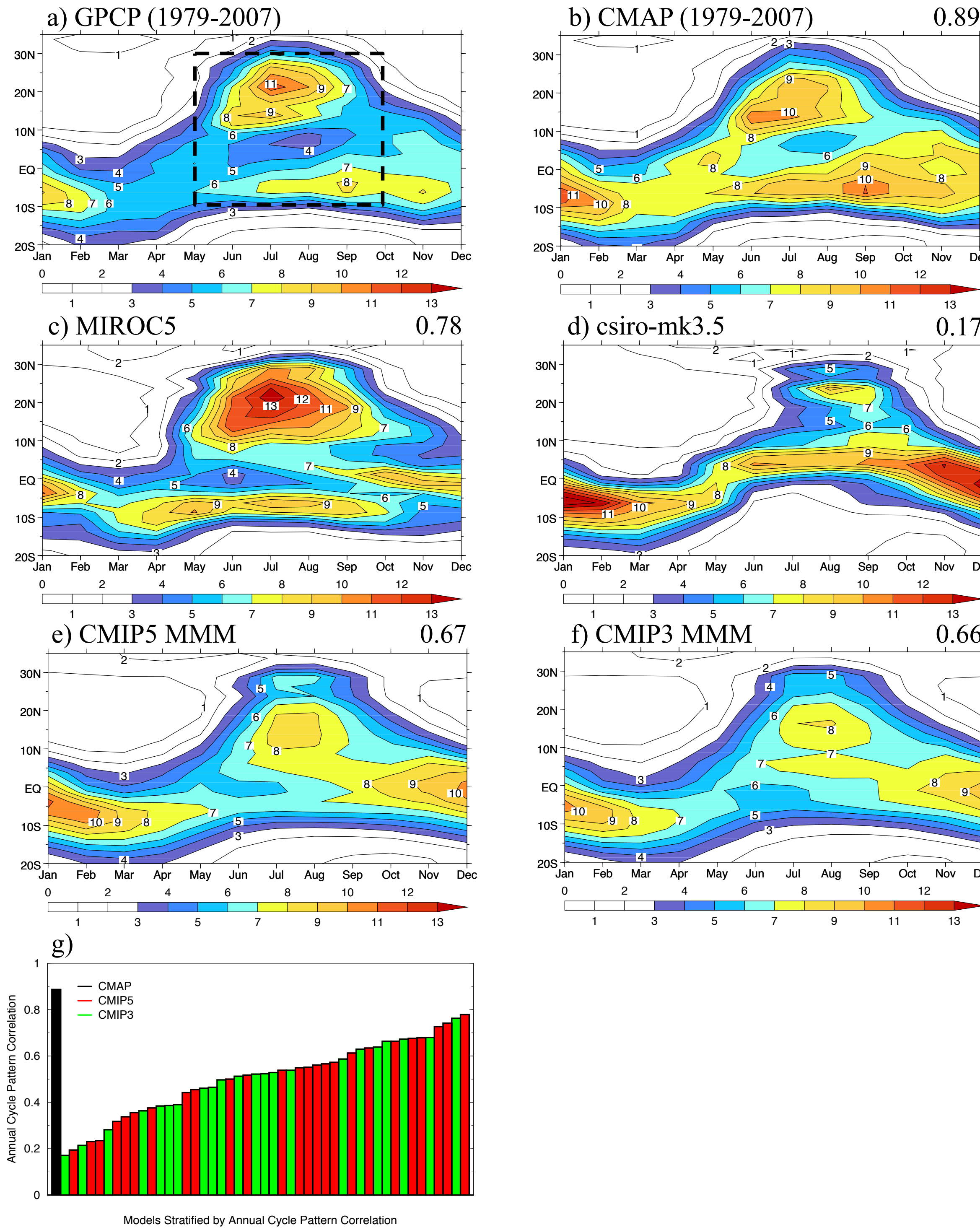

Fig. 4 a-f Annual cycle climatology for rainfall rate averaged between 70^{o}E-90^{o}E from **a** GPCP, **b** CMAP, **c** MIROC5, **d** csiro-mk3.5, **e** CMIP5 MMM, and **f** CMIP3 MMM. Also given in **b-f** is the pattern correlation with GPCP over the region 10^{o}S-30^{o}N, for May-September (the dashed region in **a**). The units are (mm day^{-1}). **g** Models stratified by their pattern correlation with GPCP. GPCP and CMAP data are from 1979-2007 and the model data is from 1961-1999

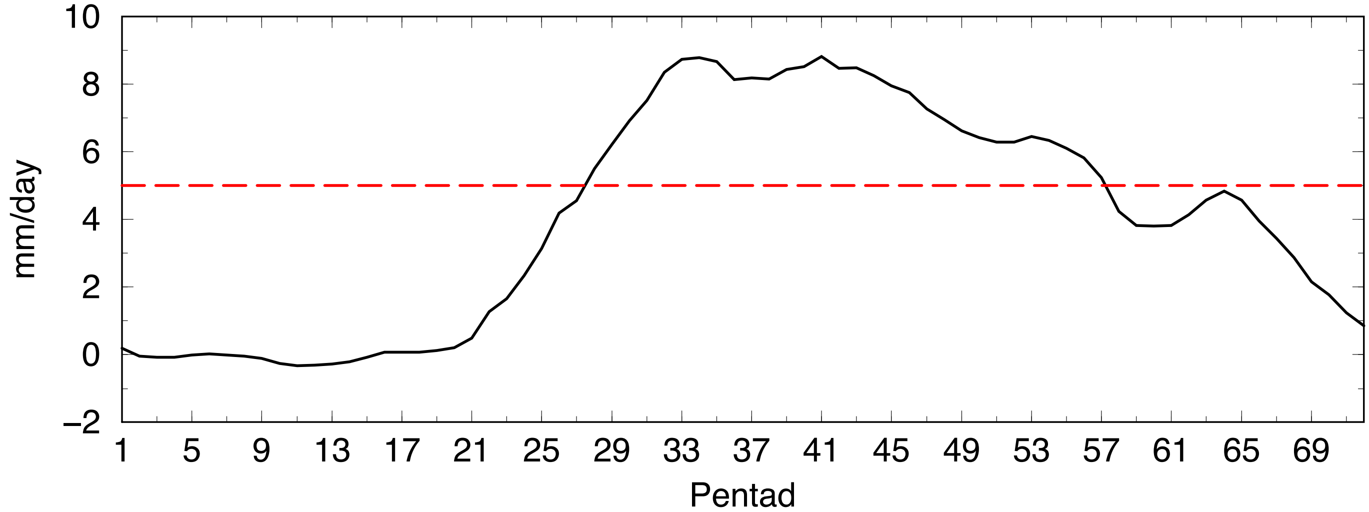

Fig. 5 The relative rainfall rate over the Bay of Bengal (85°E-90°E, 7.5°N-20°N) from GPCP data. The 5 mm day^{-1} threshold is used to define the pentads of onset and withdrawal of the monsoon. To calculate the relative rainfall rate, the pentad time series is smoothed with a five pentad running mean. The January mean rainfall is then removed from each pentad, resulting in the relative rainfall rate. See Section 4.2 for more details

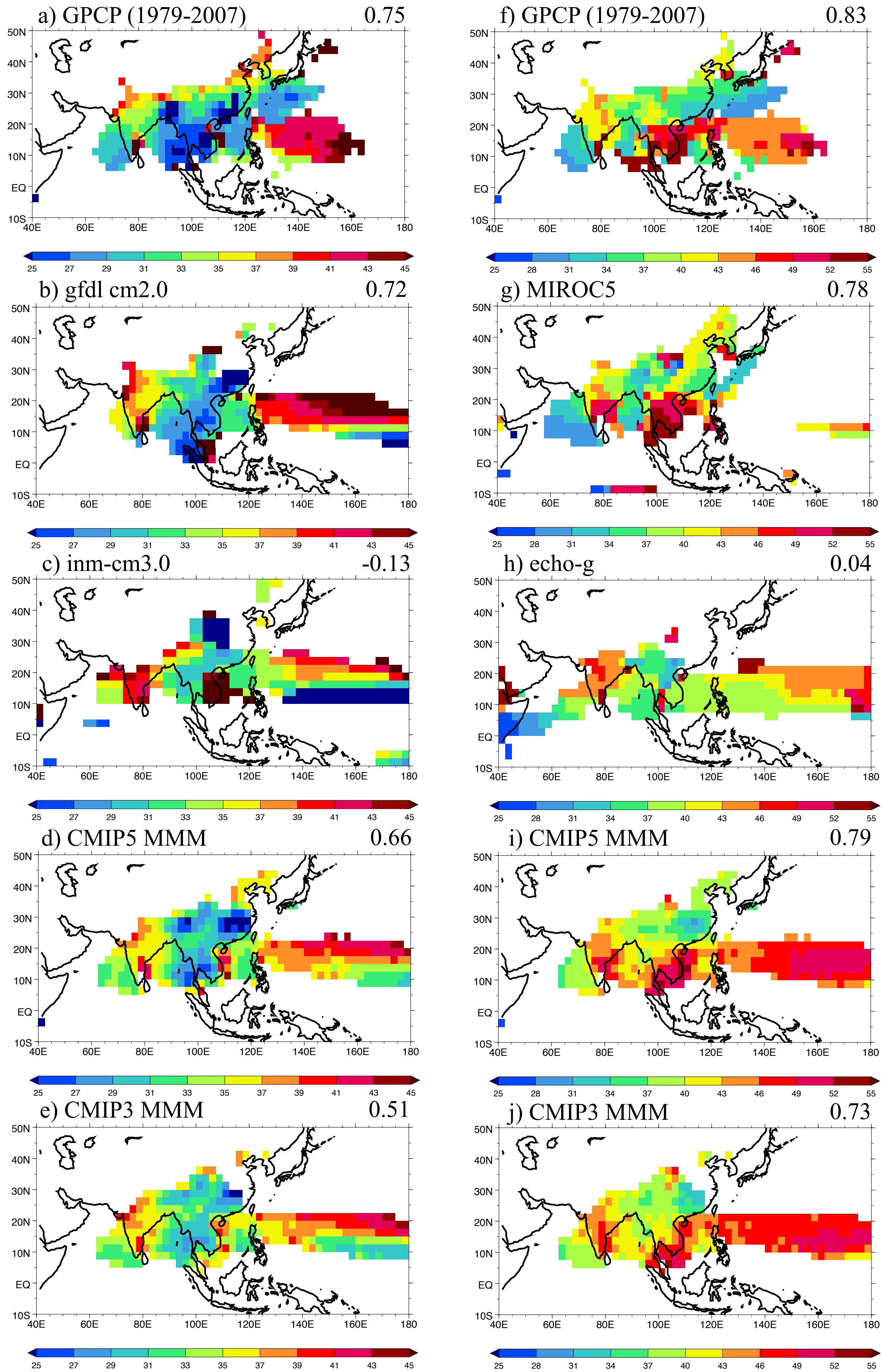

Fig. 6 Monsoon onset pentad **a** GPCP, **b** gfdl cm2.0, **c** inm-cm 3.0, **d** CMIP5 MMM, and **e** CMIP3 MMM. Monsoon peak pentad **f** GPCP, **g** MIROC5, **h** echo-g, **i** CMIP5 MMM, and **j** CMIP3 MMM. Also given in **a** and **f** is the pattern correlation of GPCP with CMAP, and in **b-e** and **g-j** are the model pattern correlations with GPCP over the region 50°E-180°E, 0°-50°N. The units are pentad (Pentad 1 = January 1-5). Note the difference in scale for the onset vs. peak phases. GPCP and CMAP data are from 1979-2007 and the model data is from 1961-1999

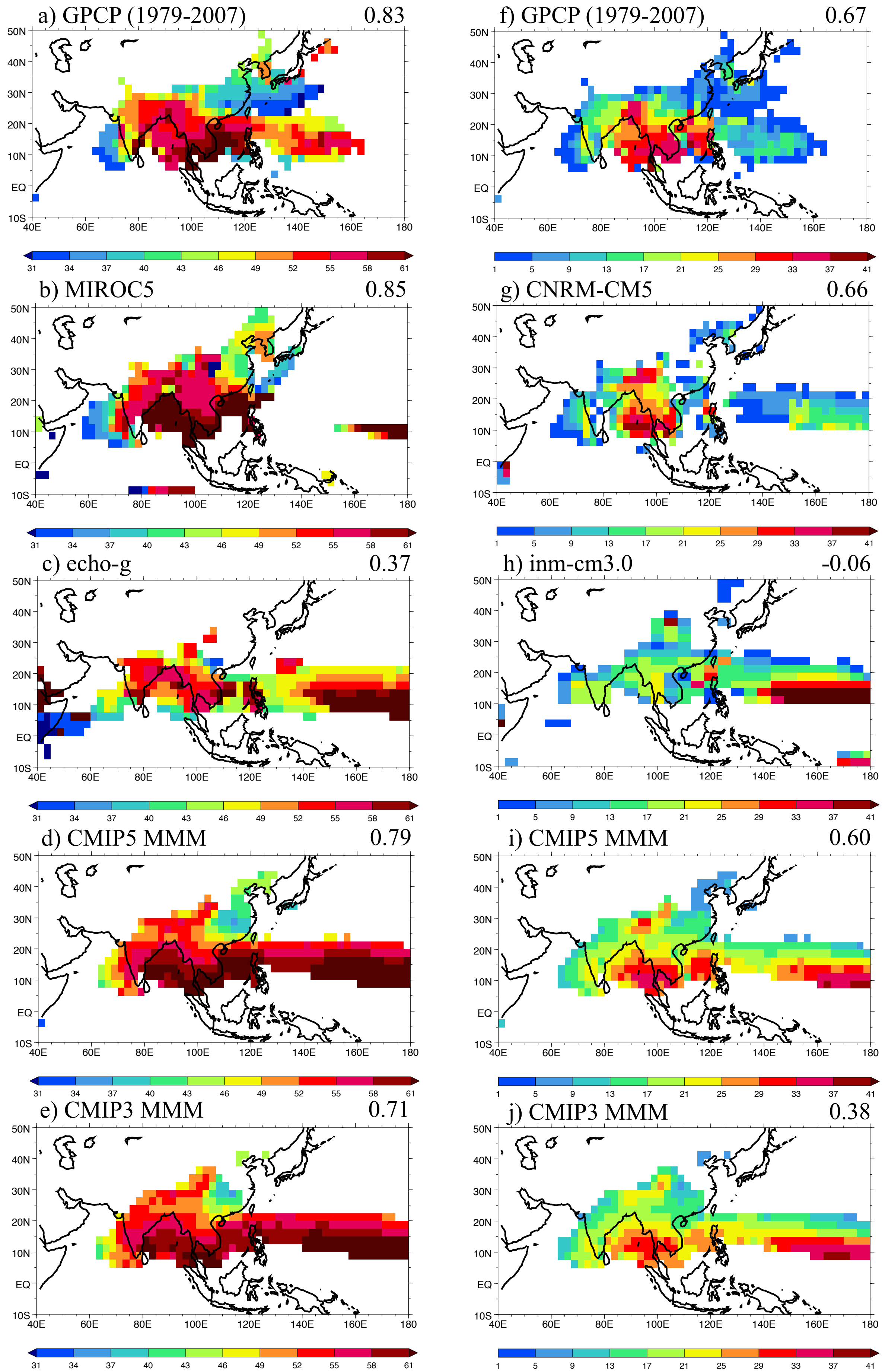

Fig. 7 Monsoon withdrawal pentad **a** GPCP, **b** MIROC5, **c** echo-g, **d** CMIP5 MMM, and **e** CMIP3 MMM. Monsoon duration **f** GPCP, **g** CNRM-CM5, **h** inm cm3.0, **i** CMIP5 MMM, and **j** CMIP3 MMM. Also given in **a** and **f** is the pattern correlation of GPCP with CMAP, and in **b-e** and **g-j** are the model pattern correlations with GPCP over the region 50°E-180°E, 0°-50°N. For withdrawal the units are pentad (Pentad 1 = January 1-5). For duration the units are the number of pentads based on (withdrawal) *minus* (onset) pentad. GPCP and CMAP data are from 1979-2007 and the model data is from 1961-1999

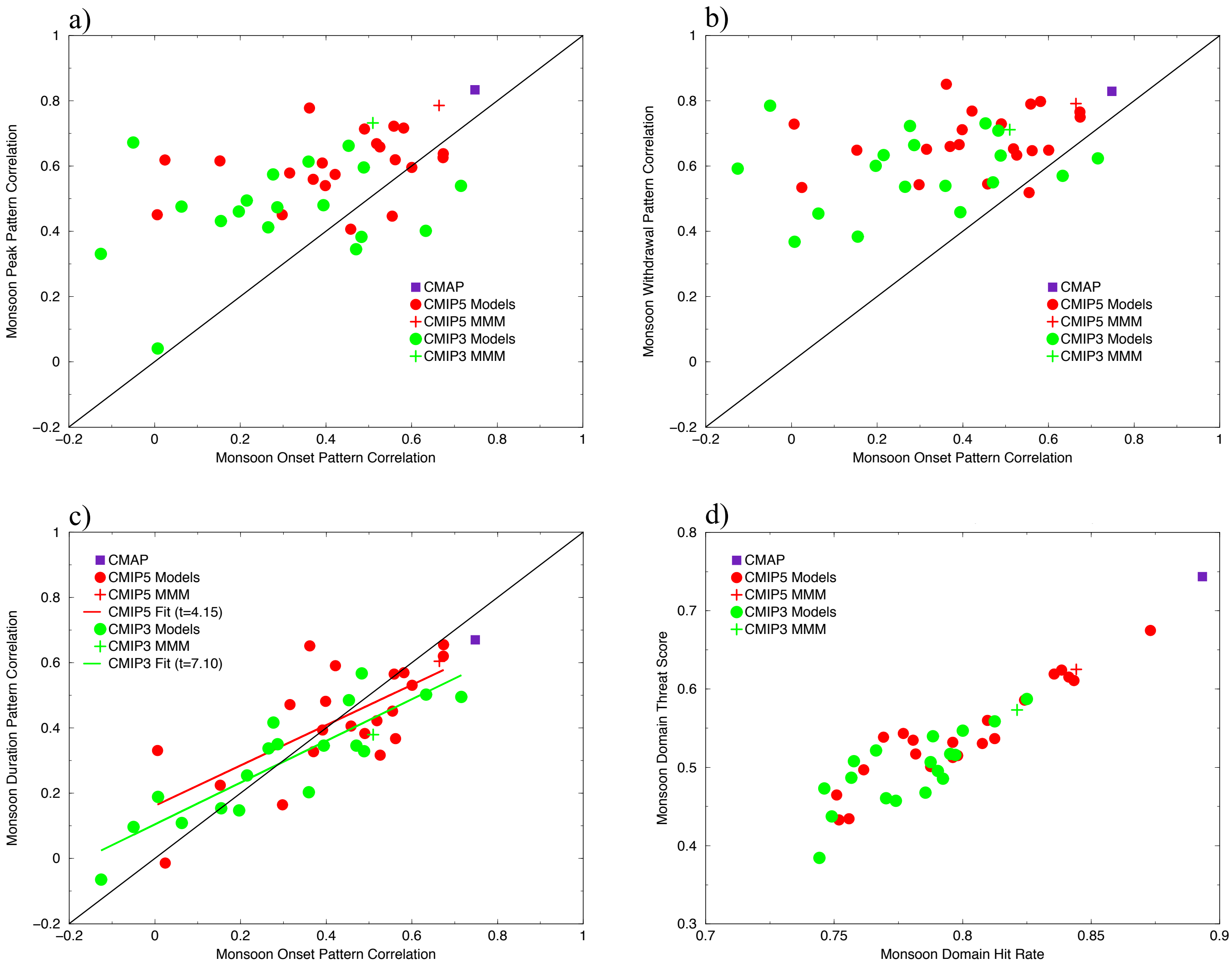

Fig. 8 Scatterplot of the pattern correlation with observations of the simulated pentad of monsoon onset vs. **a** the pattern correlation with observations of the simulated pentad of monsoon peak, **b** the pattern correlation with observations of the simulated pentad of monsoon withdrawal, and **c** the pattern correlation with observations of the simulated number of pentads of monsoon duration. **d** Scatterplot of the Monsoon Domain Hit Rate vs. the Monsoon Domain Threat Score. In **a-d** the skill is with respect to GPCP for the region 50ºE-180ºE, 0º-50ºN

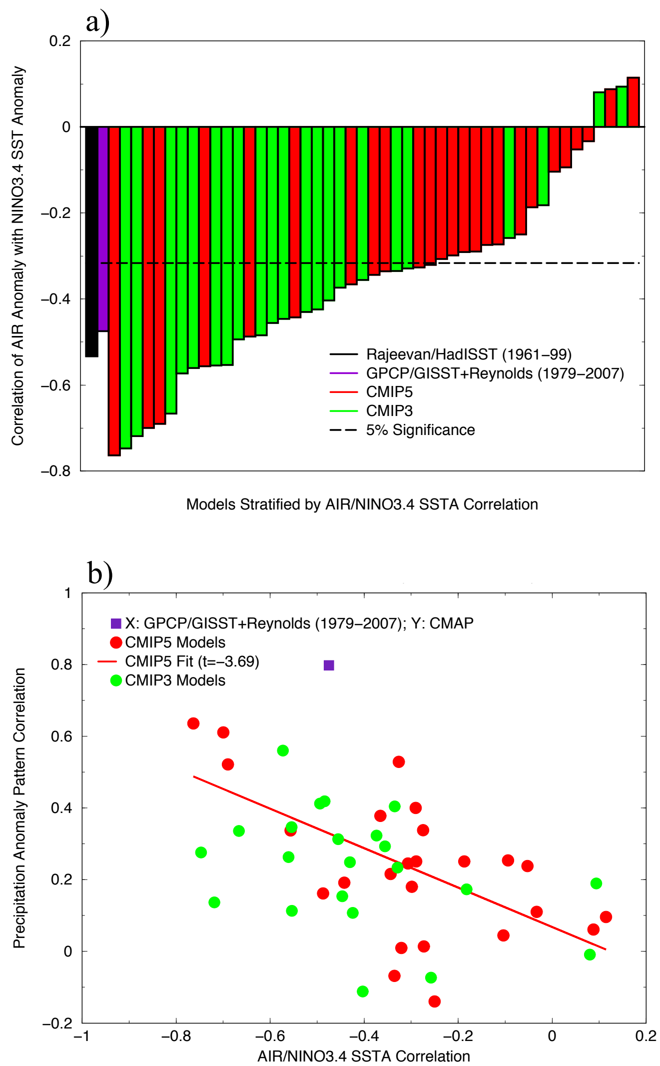

Fig. 9 **a** The ENSO-monsoon relationship skill is given by the lag 0 correlation between interannual JJAS anomalies of AIR and NINO3.4 SST. The AIR is for land-only gridpoints over 65°E-95°E, 7°N-30°N. The results are given for the Rajeevan rainfall data vs. HadISST SST (1961-1999; black), GPCP rainfall vs. SST used in the NCEP-NCAR Reanalysis (1979-2007; violet), CMIP5 models (1961-1999; red), and the CMIP3 models (1961-1999; green). The thick black dashed line is the 5% significance level assuming each year is independent for 37 degrees of freedom. **b** The AIR-NINO3.4 SST correlations in **a** are plotted vs. the pattern correlations of the interannual JJAS precipitation anomalies (mm day^{-1}) from linear regression with JJAS NINO3.4 SST anomalies (see Fig. 10). The pattern correlations are calculated with respect to GPCP over the region 60°E-100°E, 0°-30°N

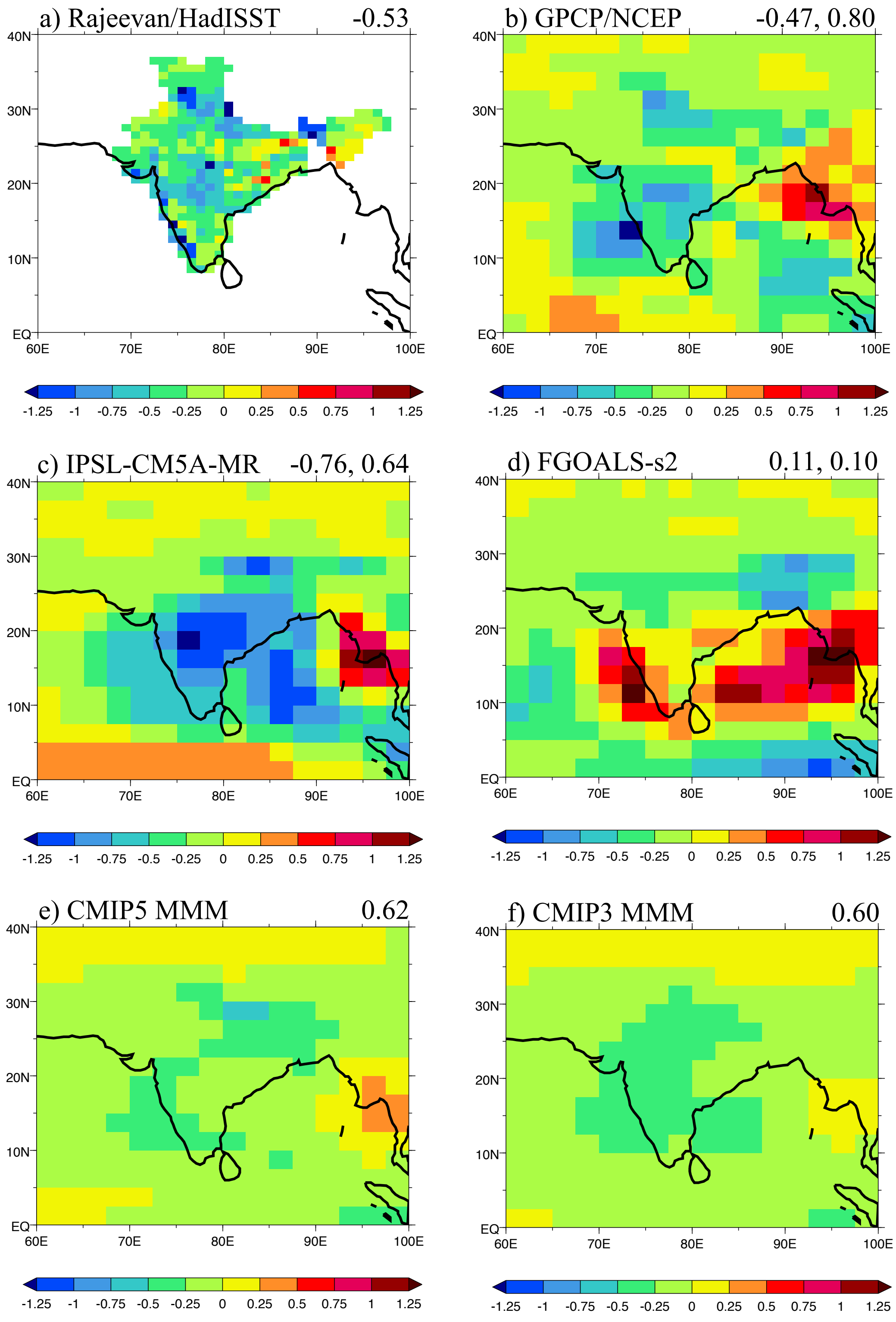

Fig. 10 Interannual JJAS precipitation anomalies (mm day^{-1}) from linear regression with JJAS NINO3.4 SST anomalies **a** Rajeevan rainfall data vs. HadISST SST (1961-1999), **b** GPCP rainfall vs. SST used in the NCEP-NCAR Reanalysis (1979-2007), **c** IPSL-CM5A-MR, **d** FGOALS-s2, **e** CMIP5 MMM, and **f** CMIP3 MMM. The regressions are scaled by one standard deviation of the NINO3.4 SST anomalies and are thus consistent with anomalies during El Nino. **c** and **d** are the models that span the range of the AIR-NINO3.4 SST correlations from the CMIP5 and CMIP3 models (see Figure 9a). In panels **a-d** the first (or only) value is the correlation of AIR-NINO3.4 SST. The last value in **b** is the pattern correlation of GPCP with CMAP for the interannual JJAS precipitation anomalies, and in **c-f** the last (or only) value is the model pattern correlation with GPCP for the interannual JJAS precipitation anomalies. The skill metrics are calculated over the region 60°E-100°E, 0°-30°N. The Rajeevan rainfall, the HadISST SST, and the model data is for 1961-1999. The GPCP, CMAP and NCEP-NCAR Reanalysis SST data are for 1979-2007

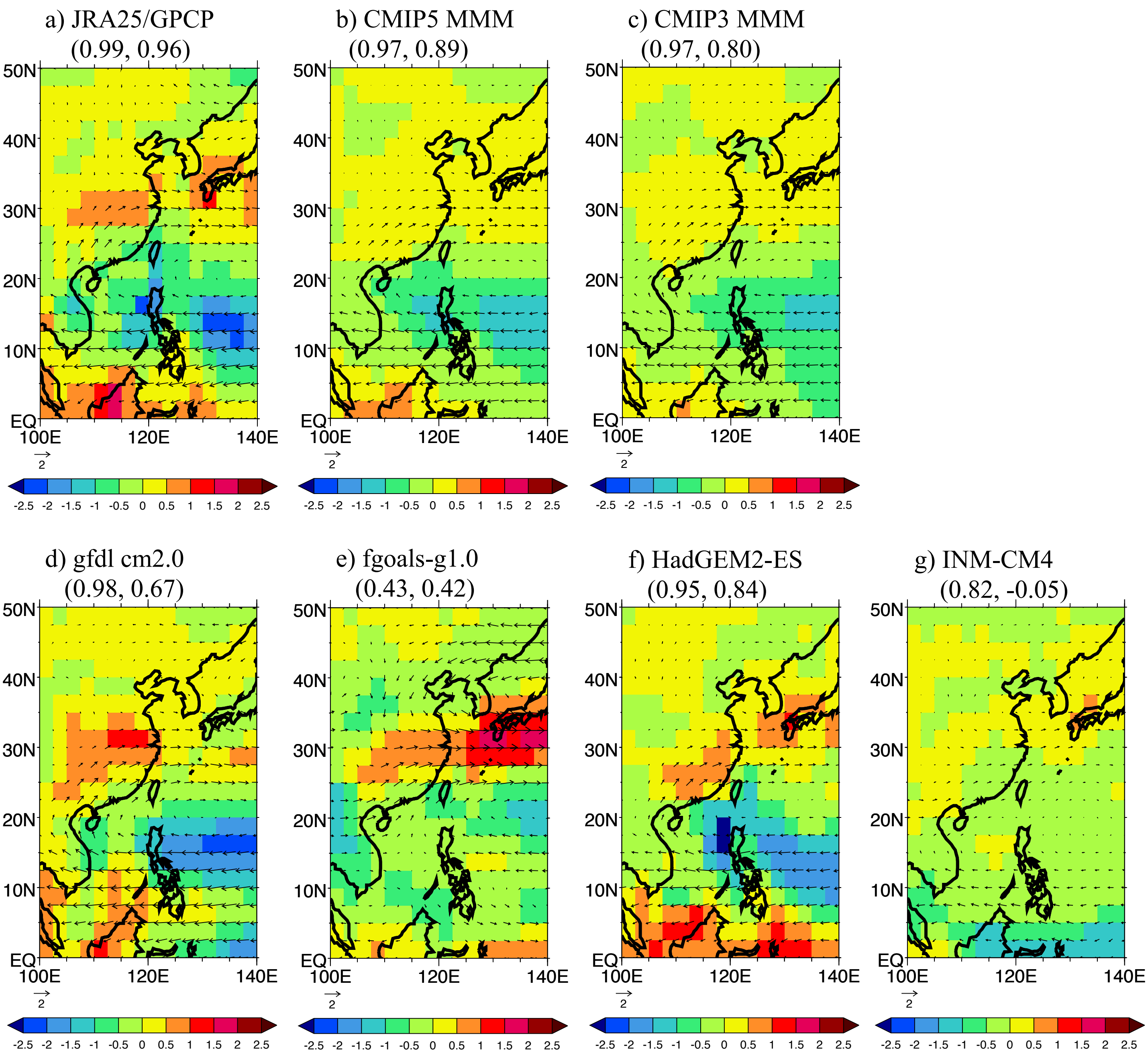

Fig. 11 Interannual East Asian summer monsoon JJA 850hPa wind anomalies and precipitation anomalies from linear regression with the revised JJA Wang-Fan 850hPa zonal wind index for **a** JRA25/GPCP, **b** CMIP5 MMM, **c** CMIP3 MMM, **d** gfdl cm2.0 model, **e** fgoals-g1.0, **f** HadGEM2-ES, and **g** INM-CM4. **d** and **e** are the models with the largest and smallest 850hPa wind pattern correlations compared to JRA25 850hPa wind anomalies, and **f** and **g** are the models with the largest and smallest precipitation pattern correlations compared to GPCP. Also given in **a** is the pattern correlation of JRA25 with NCEP/NCAR Reanalysis and GPCP with CMAP, respectively, and in **b-g** are the model pattern correlations with JRA25 and GPCP over the region 100^{o}E-140^{o}E, 0^o-50^{o}N. The units for the 850hPa wind anomalies are ms^{-1} and for precipitation anomalies the units are mm day^{-1}. The JRA25 reanalysis, the NCEP-NCAR reanalyses, the GPCP, and CMAP data are for 1979-2007. The model data is for 1961-1999

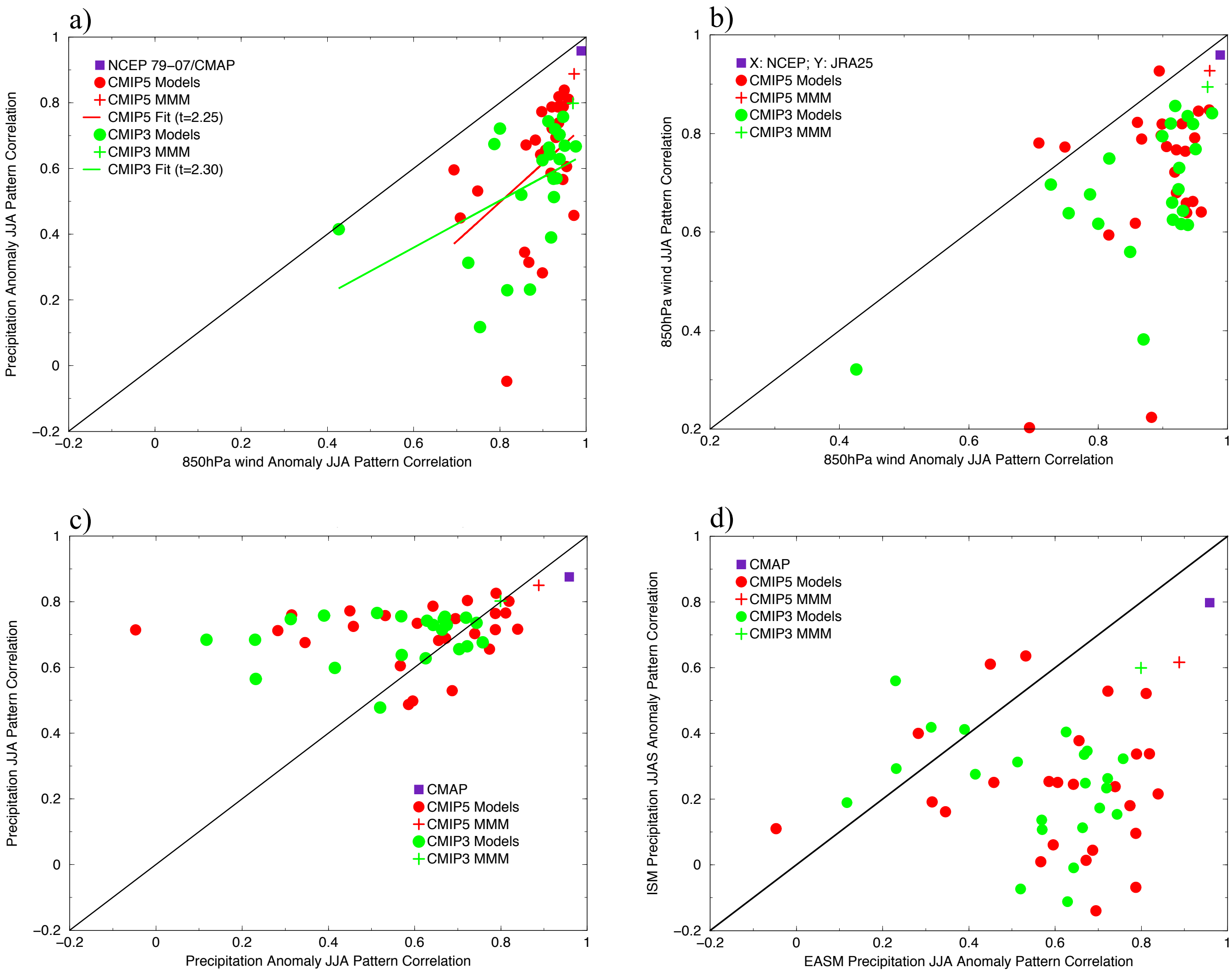

Fig. 12 **a** Scatterplot of the pattern correlation with observations of simulated JJA 850hPa wind anomalies vs. the pattern correlation with observations of simulated JJA precipitation anomalies over East Asia. The skill is relative to JRA25 and GPCP over the region 100°E-140°E, 0°-50°N. **b** Scatterplot of the pattern correlation with observations of simulated JJA 850hPa wind anomalies vs. the pattern correlation with observations of the simulated JJA 850hPa wind climatology. The skill is with respect to JRA25 on the x-axis, and with respect to ERA40 on the y-axis. **c** Scatterplot of the pattern correlation with GPCP of simulated JJA precipitation anomalies vs. the pattern correlation with observations of the simulated JJA precipitation climatology. **d** Scatterplot of the pattern correlation with GPCP of simulated JJA precipitation anomalies over the East Asia (as in Figs. 12a and 12c) vs. the pattern correlation with GPCP of simulated JJAS precipitation anomalies over the Indian Summer Monsoon (as in Fig. 9b)

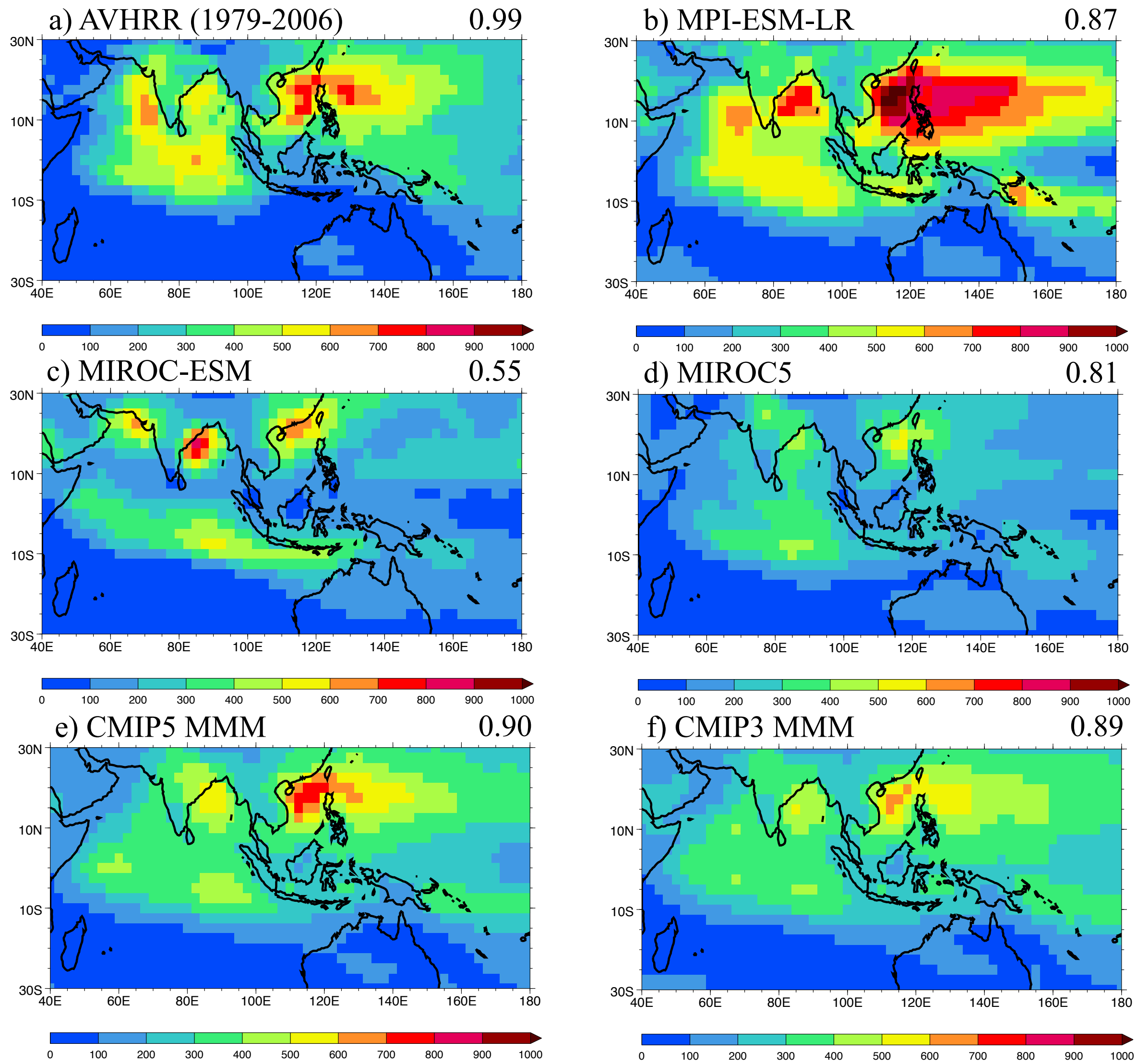

Fig. 13 20-100 day bandpass filtered OLR variance for JJAS from **a** AVHRR (1979-2006), **b** MPI-ESM-LR, **c** MIROC-ESM, **d** MIROC5, **e** CMIP5 MMM, and **f** CMIP3 MMM. Also given in **a** is the pattern correlation with AVHRR OLR for 1979-1995, and in **b-f** are the model pattern correlations with AVHRR OLR (1979-2006) over the region 40^{o}E-180^{o}E, 30^{o}S-30^{o}N. The model data is for 1961-1999.

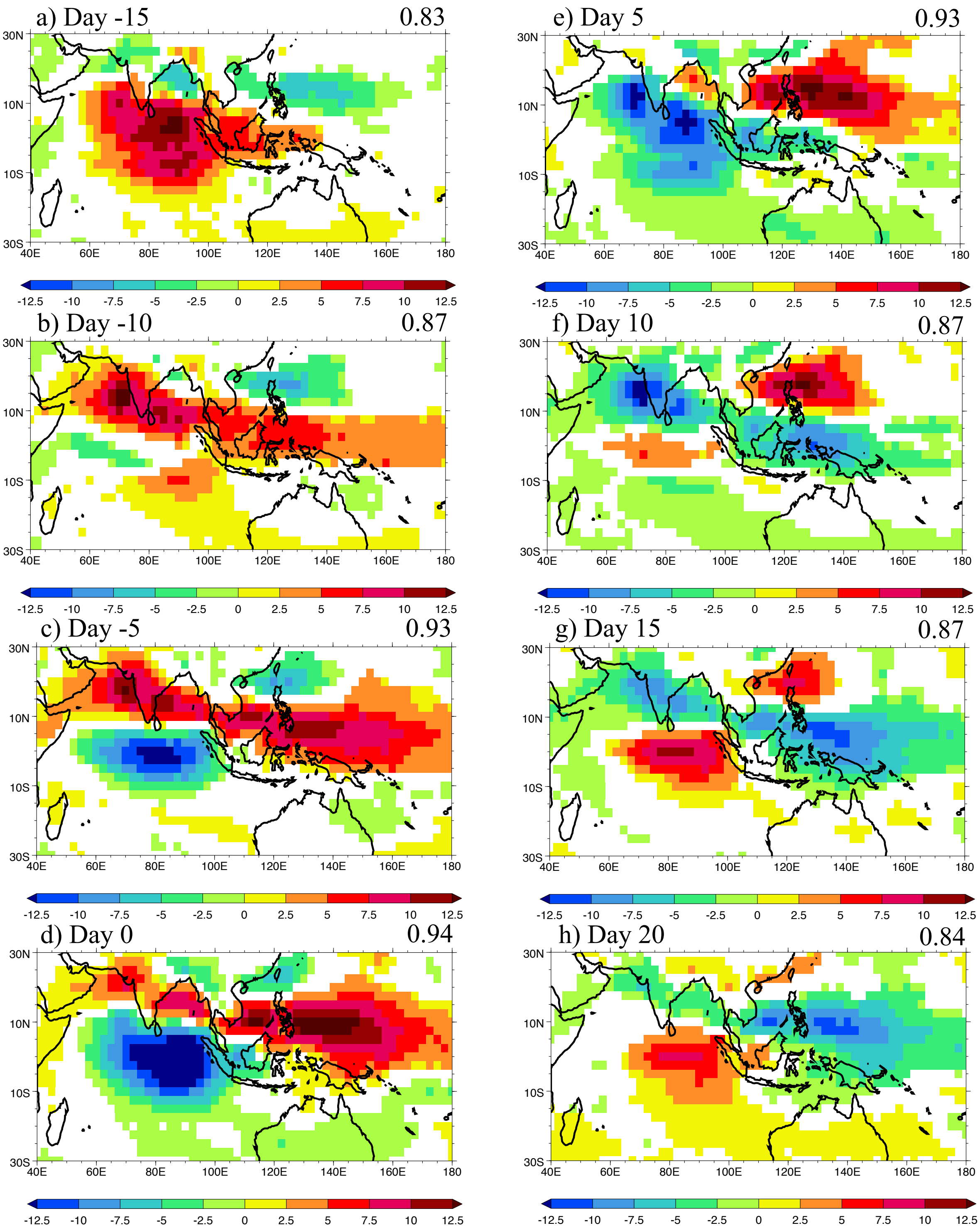

Fig. 14 Lag regression of 20-100 day bandpass filtered AVHRR OLR with PC-4 for JJAS 1979-2006 for **a** Day -15 to **h** Day 20. The lag regressions have been scaled by one standard deviation of PC-4 to give units of W m^{-2}. The pattern correlations are calculated with respect to Day -15, Day -10, Day -5, Day 0, Day 5, Day 10, Day 15, and Day 20 of the CsEOF of Annamalai and Sperber (2005) over the region 40^{o}E-180^{o}E, 30^{o}S-30^{o}N. Data are plotted where the regressions are statistically significant at the 5% level, assuming each pentad is independent

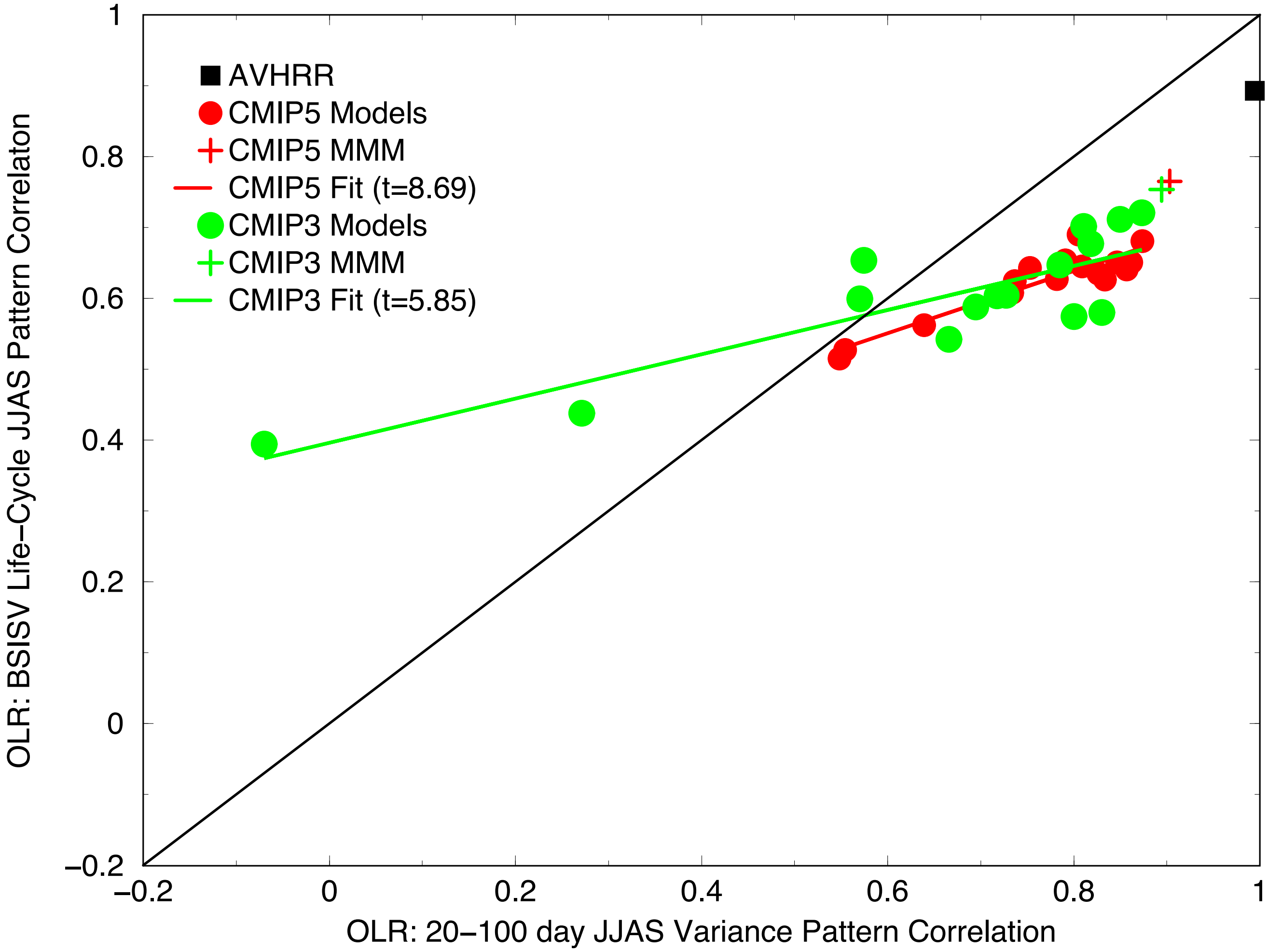

Fig. 15 Scatterplot of the pattern correlation with observations of the simulated JJAS 20-100 day bandpass filtered OLR variance vs. the space-time pattern correlation with observations of the simulated JJAS BSISV life-cycle. For the variance, the observed and simulated skill is calculated with respect to AVHRR OLR for JJAS 1979-2006. The observed variance skill is calculated using the JJAS 20-100 day bandpass filtered OLR variance for 1979-1995. For BSISV, the skill is for the models best matching patterns with respect to Day -15, Day -10, Day -5, Day 0, Day 5, Day 10, Day 15, and Day 20 of the CsEOF given in Annamalai and Sperber (2005). The observed (1979-2006) and simulated BSISV life-cycle is recovered from linear regression with PC-4 obtained by projecting 20-100 day bandpass filtered OLR onto the Day 0 CsEOF pattern from Annamalai and Sperber (2005). The skill scores are calculated over the region 40°E-180°E, 30°S-30°N

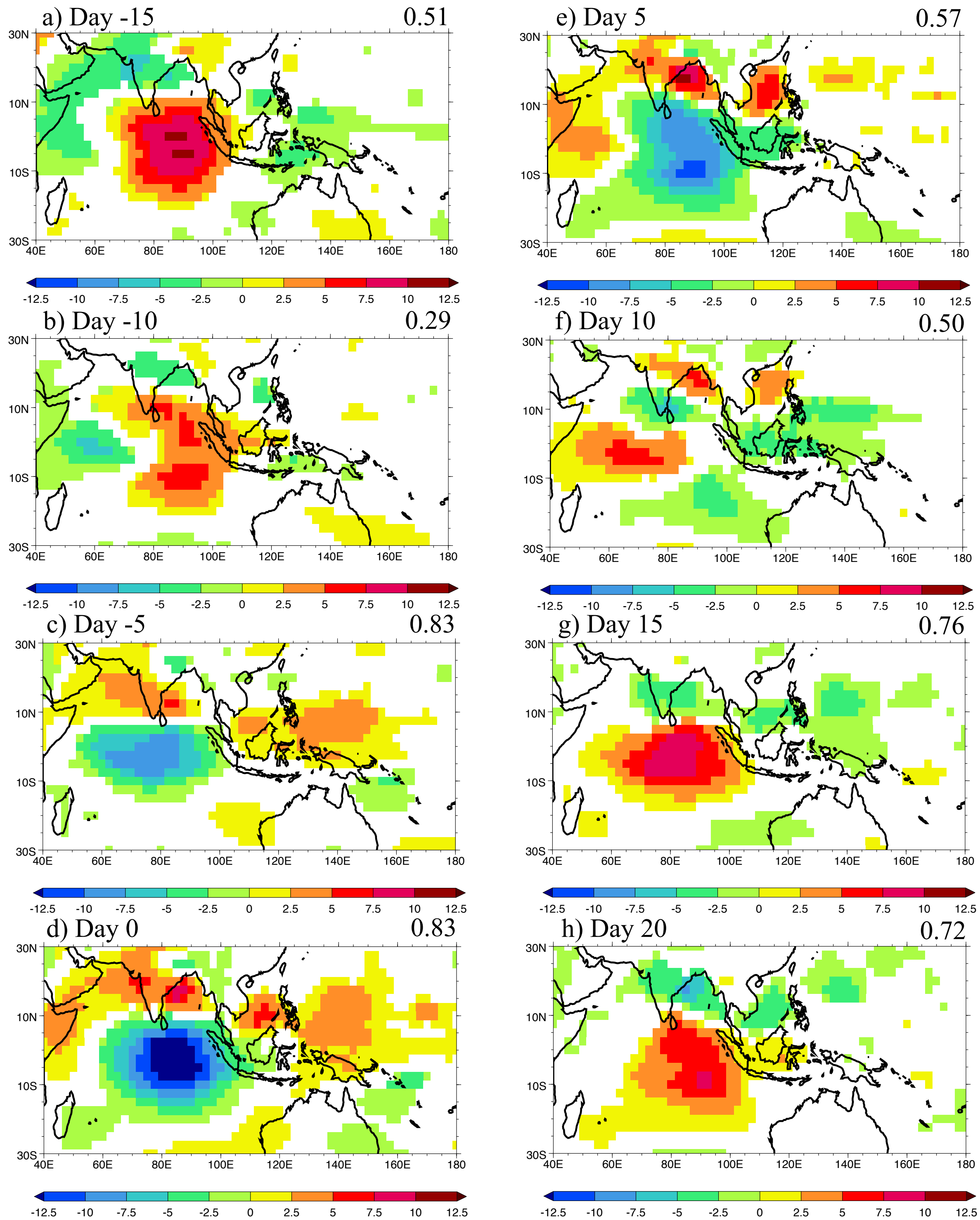

Fig. 16 As Fig. 14, but for MIROC5 20-100 day bandpass filtered JJAS OLR (1961-1999)

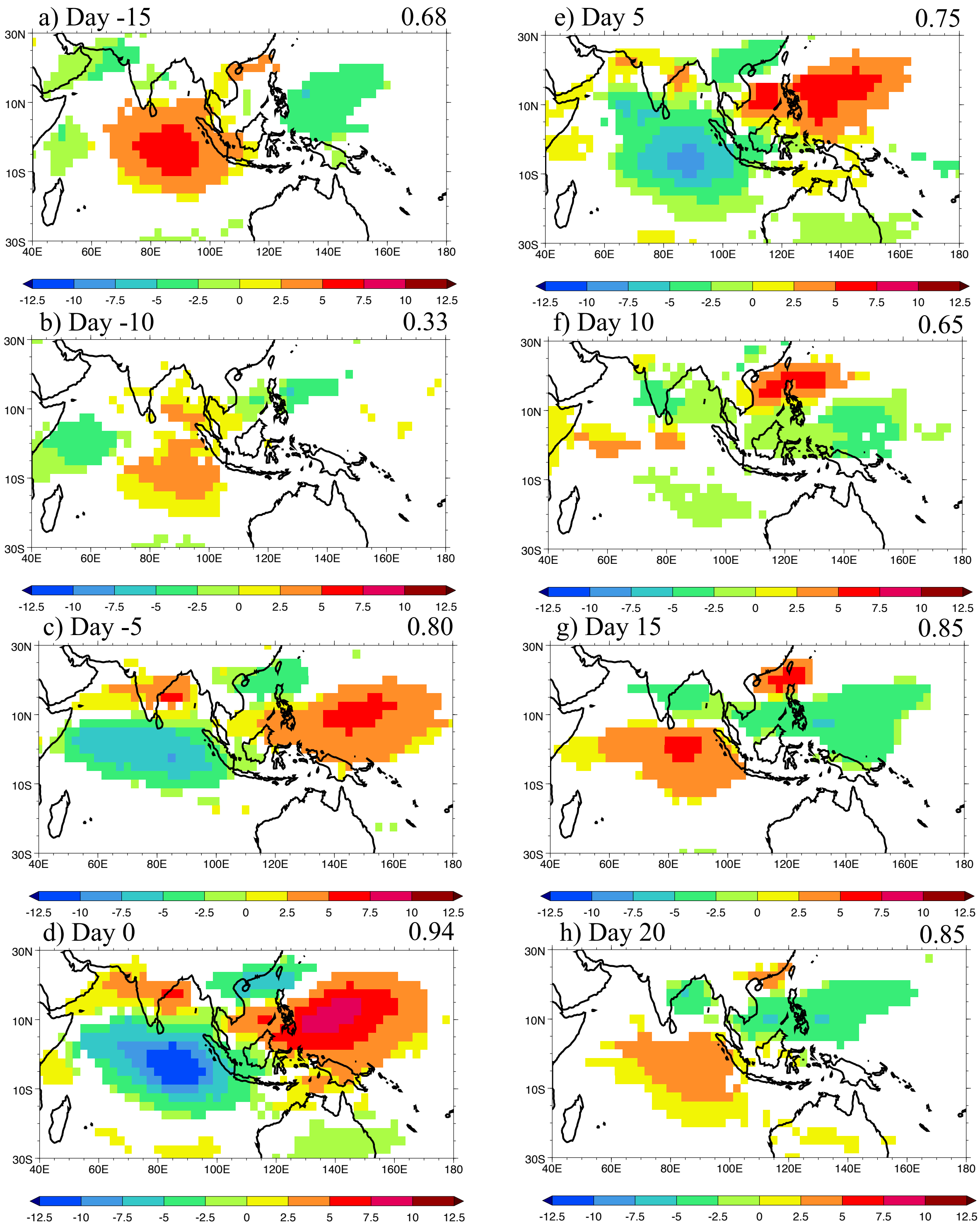

Fig. 17 As Fig. 14, but for the CMIP5 MMM. For each time lag, and at each gridpoint, the average anomaly is plotted if more than half of the models have a statistically significant convective anomaly, irrespective of sign